

Spin Dynamics of Radical Pairs

Sebastian Orbell

St John's College

University of Oxford



A Thesis Submitted for
the Honour School of Chemistry:

Chemistry Part II, 2019

Physical and Theoretical Chemistry Laboratory

Oxford, Trinity 2019

Summary

Radical pairs are molecular systems which contain two unpaired electrons and are known to be functional in many important biochemical processes including photosynthesis^{[1][2]} and possibly avian magnetoreception^{[3][4][5]}. Radical pair reactions are electron spin state selective and therefore their reactivity is dependent upon the spin dynamics of the system. The dynamics of the spin selective radical pair reactions have strong magnetic and temperature dependencies which are explored in this thesis.

A code has been developed to simulate the spin dynamics of radical pairs with a large number of nuclear spins. The size of the Hilbert space for fully quantum mechanical simulations grows exponentially with the number of coupled spins and radical pairs with more than 10 nuclear spins are infeasible to simulate using these methods. By using the Schulten-Wolynes semi-classical approximation applied to perturbative Redfield theory a new method has been devised. This method enables simulations to be performed for radical pair systems in the condensed phase while including spin selective asymmetric recombination and relaxation effects rigorously.

The computational model was parameterised for the radical pairs $DMJ - An - FN_1 - NDI$ and $DMJ - An - PE_1P - NDI$ and then used to reproduce the results from experiments conducted by Scott *et al.*^[6]. In the experimental paper a simple incoherent kinetic scheme was used to extract the temperature dependent rate constants and this thesis will highlight the importance of instead simulating these systems quantum mechanically by including the coherent evolution of the spin dynamics. The new observations and insights which have been elucidated about the magnetic field affected charge transport mechanism are then discussed. The phenomena of negatively activated recombination pathways and field independent triplet yields which were observed experimentally were confirmed using the simulations and the physical origin of these effects examined. The discussion includes a novel proposal for a model of the system with an intermediate radical state which

is supported by an analysis of the results using the Nakajima-Zwanzig equation. Finally there is a discussion of possible future work which may be motivated by the findings of this thesis.

- [1] Michael R. Wasielewski. *Journal of Organic Chemistry*, 71(14):5051–5066, 2006.
- [2] Brian Brocklehurst. *Chemical Society Reviews*, 31(5):301–311, 2002.
- [3] Hamish G. Hiscock, Daniel R. Kattnig, David E. Manolopoulos, and P. J. Hore. *Journal of Chemical Physics*, 145(12), 2016.
- [4] C. T. Rodgers and P. J. Hore. *Proceedings of the National Academy of Sciences*, 106(2):353–360, 2009.
- [5] Thorsten Ritz, Salih Adem, and Klaus Schulten. *Biophysical Journal*, 78(2):707–718, 2000.
- [6] Amy M Scott and Michael R Wasielewski. *Journal of the American Chemical Society* pages 3005–3013, 2011.

Contents

1	Introduction	1
1.1	Radical Pair Spin States	2
1.2	The radical pair mechanism	3
1.3	Probing charge transport with temperature dependence and the mag- netic field effect	4
1.4	Bio-mimetic Molecular wires	5
1.5	The challenges of modelling radical pairs	6
1.6	Outline of thesis	6
2	Theory	8
2.1	Quantum Mechanics	8
2.1.1	Quantum Master Equations	8
2.1.2	The spin Hamiltonian	9
2.1.3	The Zeeman interaction	10
2.1.4	The hyperfine interaction	10
2.1.5	The Scalar coupling interaction	11
2.1.6	The dipolar coupling interaction	12
2.1.7	The Haberkorn recombination operator	12
2.2	Semi-classical methods.	13
2.2.1	Schulten-Wolynes approximation	13
2.2.2	Redfield Theory	14
3	Implementation	19
3.1	Liouville Space	19
3.1.1	Hilbert space	19
3.1.2	Bras and Kets	19
3.1.3	Superoperators	20
3.1.4	Matrix representation	20
3.2	Monte-Carlo sampling	22
3.2.1	Sampling from the surface of a sphere	22
3.3	Matrix representation of Redfield theory	23
3.3.1	Linear algebra	24
3.3.2	The spectral density function	25
3.3.3	Observables	26

4	Molecular wires	27
4.1	Experimental results	27
4.2	Radical pair model	29
4.2.1	Rotational diffusion	30
4.2.2	Internal motion	31
4.3	Electronic transitions	31
4.3.1	Extended Marcus-Hush theory	31
4.3.2	Exponential Model	32
4.4	Triplet yield correction at high fields	33
4.4.1	Initial triplet population	33
4.4.2	Intersystem crossing	34
4.4.3	Additional spin relaxation	34
4.5	Parameterisation	34
4.5.1	Anisotropic hyperfine and g-tensor interaction terms	35
4.5.2	Dipolar coupling tensors	35
4.5.3	Frames of reference	35
4.5.4	Stokes-Einstein equation	36
4.5.5	Viscosity of toluene	37
4.6	Maximum likelihood parameter estimation	37
5	Results and discussion	40
5.1	Results	40
5.2	Discussion	45
5.2.1	Mechanisms of electron transfer	45
5.2.2	Negative activation Energy	46
5.2.3	An intermediate radical pair state	48
5.2.4	Analysis of results	51
5.2.5	Singlet-Triplet dephasing mechanism	53
5.2.6	Triplet yield correction at high fields	54
6	Conclusion and Future work	57
	References	58
A	Redfield theory in Liouville space	61
B	Extended Marcus-Hush theory	63
C	Summary of models	65

D Parameters from DFT calculations	73
D.1 Rotational diffusion	73
D.2 Dipolar coupling tensors	73
D.3 G-tensors	74
D.4 Hyperfine tensors	75



FINAL HONOUR SCHOOL OF CHEMISTRY

DECLARATION OF AUTHORSHIP

[Instructions to candidates.]

Name (in capitals):

Candidate number:

College (in capitals):

Supervisor:

Title of thesis (in capitals):

Please tick to confirm the following:

I have read and understood the University's disciplinary regulations concerning conduct in examinations and, in particular, the regulations on plagiarism (*The University Student Handbook* Section 8.8; available at <https://www.ox.ac.uk/students/academic/student-handbook?wssl=1>). ☐

I have read and understood the Education Committee's information and guidance on academic good practice and plagiarism at <https://www.ox.ac.uk/students/academic/guidance/skills> ☐

The thesis I am submitting is entirely my own work except where otherwise indicated. ☐

It has not been submitted, either partially or in full, either for this Honour School or qualification or for another Honour School or qualification of this University (except where the Special Regulations for the subject permit this), or for a qualification at any other institution. ☐

I have clearly indicated the presence of all material I have quoted from other sources, including any diagrams, charts, tables or graphs. ☐

I have clearly indicated the presence of all paraphrased material with appropriate references. ☐

I have acknowledged appropriately any assistance I have received in addition to that provided by my supervisor. ☐

I have not copied from the work of any other candidate. ☐

I have not used the services of any agency providing specimen, model or ghostwritten work in the preparation of this thesis. (See also section 2.4 of Statute XI on University Discipline under which members of the University are prohibited from providing material of this nature for candidates in examinations at this University or elsewhere: <http://www.admin.ox.ac.uk/statutes/352-051a.shtml>) ☐

I agree to retain an electronic copy of this work until the publication of my final examination result, except where submission in hand-written format is permitted. ☐

I agree to make any such electronic copy available to the examiners should it be necessary to check for plagiarism. ☐

Candidate's signature:Date:

Acknowledgements

First and foremost, I thank my supervisor Prof. David Manolopoulos for his enthusiasm and support throughout the year. I also thank Willem van Heusde, Joe Lawrence, Lachlan Lindoy and Tom Fay for all their invaluable help, guidance and patience in addition to their company during many entertaining coffee breaks. I would particularly like to express my gratitude to Tom Fay for assisting me throughout the year in addition to proof reading this thesis.

I thank my undergraduate tutors Angela Russel, Richard Compton and Fraser Armstrong for the excellent teaching and support they provided me for the duration of my undergraduate degree. Lastly I thank my family and close friends for their unceasing love and support. I thank all the friends I have made during my time in Oxford, it has been an absolute privilege to spend time with them over the last four years.

Abbreviations

MFE	Magnetic Field Effect
MARY	Magnetically Affected Reaction Yield
DFT	Density Functional Theory
EPR	Electron Paramagnetic Resonance
RP	Radical Pair
ISC	Interstystem Crossing
HOMO	Highest Energy Molecular Orbital
NSE	Nash–Sutcliffe model efficiency coefficient
B	External magnetic field
J	Electron-electron coupling constant
S	Electron spin quantum number
I	Nuclear spin quantum number
\hbar	Reduced Plank constant $(\hbar = \frac{h}{2\pi} = 1.0545718 \times 10^{34} \text{ kg m}^2 \text{ s})$
π	Pi ($\pi = 3.1415..$)
\hat{H}	Hamiltonian operator
\mathcal{L}	Liouville superoperator
$\hat{\rho}$	Density operator
eV	Electron Volts
mT	Milli Tesla
ns	Nano Seconds
kJ mol^{-1}	Kilo Joule per Mole
nm	Nano Metre
FN_1	$DMJ - An - FN_1 - NDI$
PE_1P	$DMJ - An - PE_1P - NDI$

Chapter 1

Introduction

Radical pairs are molecular systems which contain two unpaired electrons and are known to be important in many systems in biology, chemistry and materials science. These include photochemical transitions and electron transfers in photosynthetic reaction pathways^{[1][2]}. Radical pairs in proteins are hypothesised to be crucial in the mechanism of avian magnetoreception and thus the effect of a magnetic field on these reactions is of great interest^{[3][4][5]}. Radical pair reactions are spin selective and therefore depend upon the spin dynamics. The development of a greater understanding of the spin selective reactivity^{[7][8]} and the factors which influence the evolution of the spin dynamics is therefore crucial for the design of biomimetic molecules which could have important technological uses^{[1][9]}.

The fundamental physical principles which govern the spin dynamics of radical pairs are quantum mechanical in nature^{[7][8]} and therefore, if a model is to accurately reproduce the evolution of such a system, it must include quantum phenomena. The focus of this thesis is to develop the theoretical and computational methods required to accurately simulate the coherent spin dynamics of a radical pair system. The underlying physical properties and mechanisms of the electronic transitions, as well as the spin relaxation mechanisms, will be probed by analysing the experimental temperature and magnetic field dependence of radical reactions, with these methods.

Most biological radical pair systems are found in the condensed phase, where magnetic interactions are modulated in a time-dependent manner as a result of internal and rotational motions of the molecules and therefore these spin relaxation mechanisms have to be incorporated into simulations. Most biologically relevant radical pairs typically have more than 10 nuclear spins so that simulating them quantum mechanically becomes intractable. Instead semi-classical and perturbative approximations which do not scale exponentially will be used to efficiently model

the spin dynamics of radical pairs.

1.1 Radical Pair Spin States

Electrons and nuclei have an intrinsic angular momentum which arises from the solution of the relativistic Schrödinger equation^[10]. This property is called spin and it has no classical analogue. Spin states, $|\phi\rangle$, are simultaneous eigenstates of the total spin angular momentum operator \hat{S}^2 and the projection operator \hat{S}_z and as such can be described by two quantum numbers $|\phi\rangle \equiv |S, M_S\rangle$. These operators and their respective eigenvalues are given by

$$\hat{S}^2 |S, M_S\rangle = 2S(S+1) |S, M_S\rangle \quad (1.1)$$

$$\hat{S}_z |S, M_S\rangle = M_S |S, M_S\rangle. \quad (1.2)$$

A single electron has $S = \frac{1}{2}$ and can therefore exist in two distinct spin states; $|\alpha\rangle \equiv |\frac{1}{2}, +\frac{1}{2}\rangle$ and $|\beta\rangle \equiv |\frac{1}{2}, -\frac{1}{2}\rangle$. Since spins are angular momenta, they can couple and, for example, two electron spins, \mathbf{S}_1 and \mathbf{S}_2 , can couple to produce a total angular momentum \mathbf{S} , which may have a spin quantum number of either $S = 1$ or $S = 0$ ^[7]. If $S = 1$ there are three corresponding states $M_S = -1, 0, 1$, denoted triplet states and these are symmetric to electron permutation. There is only one state with the value $S = 0$ ($M_S = 0$) which is denoted the singlet state and is anti-symmetric to electron permutation. The coupled states can be expressed in terms of uncoupled spin states as^[7]

$$|T_+\rangle \equiv |1, 1\rangle \equiv |\alpha\rangle_1 \otimes |\alpha\rangle_2 \quad (1.3)$$

$$|T_0\rangle \equiv |1, 0\rangle \equiv \frac{1}{\sqrt{2}} \left(|\alpha\rangle_1 \otimes |\beta\rangle_2 + |\beta\rangle_1 \otimes |\alpha\rangle_2 \right) \quad (1.4)$$

$$|T_-\rangle \equiv |1, -1\rangle \equiv |\beta\rangle_1 \otimes |\beta\rangle_2 \quad (1.5)$$

$$|S\rangle \equiv |0, 0\rangle \equiv \frac{1}{\sqrt{2}} \left(|\alpha\rangle_1 \otimes |\beta\rangle_2 - |\beta\rangle_1 \otimes |\alpha\rangle_2 \right). \quad (1.6)$$

Since electrons are fermions their total electronic wavefunction must be anti-symmetric with respect to electron permutation and consequently triplet states must have anti-symmetric spatial wavefunction components and similarly for a singlet

state the spatial component of the total wavefunction must be symmetric. The electronic states defined by these distinct total wavefunctions will consequently have different eigenvalues under the Hamiltonian for the system^[8].

Generally, in radical pair reactions the spin orbit coupling, as well as the coupling of electron spins to nuclear degrees of freedom, are weak or negligible. Therefore, despite the energy difference between spin states being orders of magnitude smaller than the thermal energy at room temperature^[8], the rate and yield of a radical pair reaction may be governed by the requirement for the conservation of spin angular momentum and will therefore be dependent upon the spin state.

1.2 The radical pair mechanism

This thesis is concerned with the study of a class of reactions which proceed via the radical pair mechanism. For the purposes of this discussion the molecular wires, in which these reactions occur, will be described by a donor-bridge-acceptor system (D-B-A) where the donor, bridge and acceptor are constituent segments of the molecule.

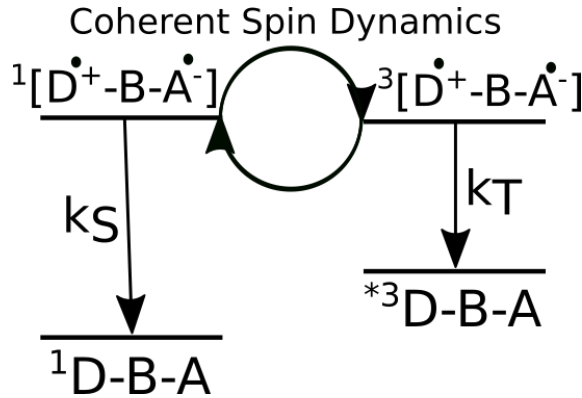


Figure 1.1: Electronic transitions in the general radical pair mechanism.

Figure 1.1 displays the principle photophysical and electronic transitions which occur for the general case of the radical pair mechanism^{[7][8]}. Photo-induced electron transfer (PET) initialises the reaction, forming an excited state which subsequently undergoes charge separation at a rate k_{CS} to form a singlet charge separated state $^1(D^{\cdot+} - B - A^{\cdot-})$.

The singlet charge separated state and the corresponding triplet state $^3(D^{\cdot+} - B - A^{\cdot-})$ then undergo coherent interconversion processes. Radical pair recombination then occurs in the singlet state via electron transfer (at a rate k_S) to form the molecule's electronic ground state. The charge separated triplet state undergoes radical pair recombination at a rate k_T . Often the resulting excited triplet state is sufficiently long lived that it can be detected experimentally.

1.3 Probing charge transport with temperature dependence and the magnetic field effect

It is known that the Cartesian components of a particle's magnetic dipole can be defined in terms of the particle's Pauli spin matrices and a constant of proportionality, γ , which is denoted the magnetogyric ratio. The magnetic dipole moment components are given by

$$\hat{\mu}_x = \gamma \hat{s}_x \quad \hat{\mu}_y = \gamma \hat{s}_y \quad \hat{\mu}_z = \gamma \hat{s}_z. \quad (1.7)$$

Hence the spins will interact with external magnetic fields as well as with other spins via magnetic interaction mechanisms. These interactions mediate the interconversion of singlet and triplet states of the radical pair which sets up a system with coherent spin dynamics. Due to the spin selectivity of the reactions and the magnetic field effect (MFE) on the dynamics, the strength of the external magnetic field and the modulation of internal fields will affect the rate and product distribution of radical pair reactions.

The degeneracy of the triplet energy states is lifted upon the addition of a magnetic field to the system^[1], as shown in figure 1.2. Therefore the energies of the states as a function of the external field are given by

$$E_{T_{\pm 1}}(B) = E_{T_{\pm 1}}(B = 0) \pm \gamma_e B \quad (1.8)$$

$$E_{T_0}(B) = E_{T_0}(B = 0). \quad (1.9)$$

Consequently the MFE on properties of the reaction such as the lifetime of the radical pair or the distribution of product yields acts as a useful probe to investigate

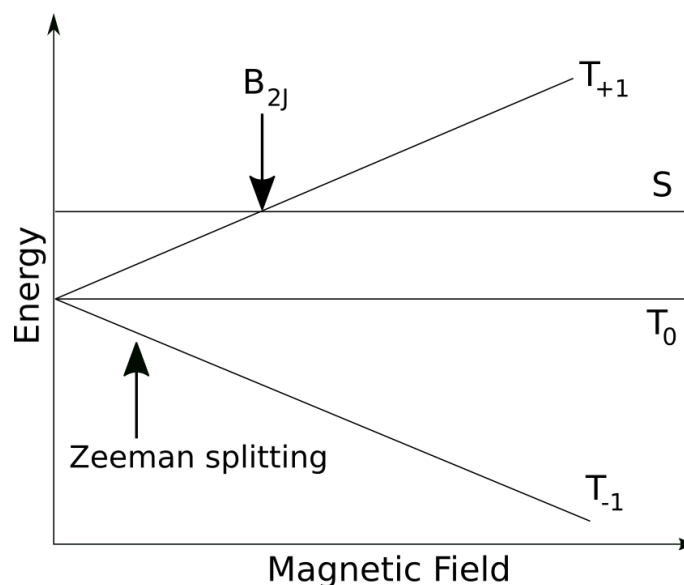


Figure 1.2: Zeeman Splitting.

the coherent dynamics of the singlet-triplet interconversion mechanism^{[11] [9] [12] [13] [14]}. Furthermore the dependence of this MFE on temperature can be used to gain insights about the properties of electronic transitions and elucidate more fundamental properties of the system dynamics such as charge transport mechanisms and free energy changes including activation energies for electronic transitions.

1.4 Bio-mimetic Molecular wires

Molecular wires were initially devised as components to conduct electrons in nanoscale devices which are being developed as Moore's law drives the need for single molecule scale transistors^[15]. The design of these molecular wires was bio-mimetic, inspired by the highly efficient processes of charge separation and charge transport observed within molecules during photosynthesis^[1]. The development of an understanding of how the molecular design affects the physical properties of these systems^{[9] [11] [6]} is of great importance in furthering the effort to create molecular wires to act as artificial photosynthetic devices for solar energy conversion.

1.5 The challenges of modelling radical pairs

Biological and bio-mimetic radical pair systems tend to have a large number of nuclear spins coupled to the electron spins. The wavefunction of such a system with N coupled spins is in the full Hilbert space, $\mathcal{H}^{(N)}$, defined by the tensor product of N Hilbert spaces given by

$$\mathcal{H}^{(N)} = \otimes_{i=1}^N \mathcal{H}_i. \quad (1.10)$$

The dimensionality of the full Hilbert space increases exponentially with the number of coupled spins and for a system of spin $\frac{1}{2}$ particles the size of the Hilbert space is n where $n = \prod_{i=1}^N n_i = 2^N$. For systems with more than about 20 coupled spins the size of the Hilbert space ($n = 2^{20} \approx 10^6$) is so large that fully quantum mechanical simulations become impractical due to their computational expense and alternative methods are required to calculate properties of the system. Semi-classical methods as well as perturbative Redfield theory are employed in this thesis to efficiently construct simulations of systems with a large number of coupled nuclear spins.

1.6 Outline of thesis

This thesis aims to develop theoretical and computational models to simulate spin dynamics of large organic radical pairs with many nuclear spins. Using the static-bath (or Schulten Wolynes) approximation applied to Redfield theory a new method has been devised in which these calculations can be performed for radical pairs with spin selective asymmetric recombination. The model contains free parameters which will be fitted to experimental results and used to elucidate physical properties of the systems such as activation energies of electronic transitions. The experimental studies, which the simulations will be compared to, were conducted in solution and therefore the associated relaxation mechanisms will be included in the calculations.

Chapter 2 reviews the theory required to model these systems quantum mechanically and introduces the semi-classical methodologies which will be used to reduce the computational expense of the calculations. Chapter 3 introduces the mathematical formalism of Liouville space and explains how the semi-classical and quantum mechanical models can be implemented in terms of matrix-vector operations so that the calculations can be conducted computationally.

Chapter 4 first describes the specific radical pair systems which will be modelled and outlines the experiments performed by Scott *et al.* on them, which the simulations aim to replicate. The methods used to explicitly include parameters unique to each radical pair system are then detailed. The method of maximum likelihood estimation used to parameterise the model is described, followed by a brief outline of the differential evolution algorithm.

Chapter 5 reviews the success of the model in reproducing experimental results and subsequently discusses the physical significance of the findings. The large quantitative and qualitative discrepancies between the temperature dependent rate constants extracted using this coherent model for the spin dynamics and the far simpler incoherent kinetic scheme used in the experimental work are highlighted. This discussion includes a novel proposal for a model of the system with an intermediate radical state which is supported by an analysis of the results using the Nakajima-Zwanzig equation. Chapter 6 concludes the thesis and offers suggestions for future work motivated by the observations which have been made.

Chapter 2

Theory

2.1 Quantum Mechanics

2.1.1 Quantum Master Equations

In experimental procedures it is rare to take measurements on single particles and in general the measurements are made on an ensemble of molecules. As a result it is necessary, in quantum mechanical calculations, to define an ensemble average of an observable $O(t)$ corresponding to an operator \hat{O} , such that

$$O(t) = Tr[\hat{\rho}(t)\hat{O}], \quad (2.1)$$

where the trace is taken over the entire Hilbert space and $\hat{\rho}(t)$ is the time-dependent density operator.

All ensemble averages of observables can therefore be calculated from the spin density operator. For the purposes of this thesis, the observables of interest are the singlet and triplet quantum yields of a radical pair recombination reaction,

$$\phi_S = k_S \int_0^\infty Tr[\hat{P}_S \hat{\rho}(t)] dt \quad (2.2)$$

$$\phi_T = k_T \int_0^\infty Tr[\hat{P}_T \hat{\rho}(t)] dt \quad (2.3)$$

where $\phi_S + \phi_T = 1$, and the radical pair lifetime,

$$\tau_{RP} = \int_0^\infty Tr[\hat{\rho}(t)] dt \quad (2.4)$$

where \hat{P}_S and \hat{P}_T are spin projection operators and k_S and k_T are singlet and triplet recombination rates respectively. In order to calculate these observables it is first necessary to simulate the evolution of the density operator

If the evolution of a system is Markovian then coherent spin dynamics can be modelled using a differential equation which is called the quantum master equation. The principle assumption of the Markovian approximation is that the correlation

functions of the nuclear motions that influence the spin dynamics decay very rapidly. This implies that no memory effects influence the evolution of the spin system. In this thesis the master equation is defined by

$$\frac{d}{dt}\rho(t) = \mathcal{L}_0\rho(t) + \mathcal{L}_V(t)\rho(t) \quad (2.5)$$

where $\mathcal{L}_0 = -\frac{i}{\hbar}[\hat{H}_0, \cdot] - \{\hat{K}, \cdot\}$ and $\mathcal{L}_V(t) = -\frac{i}{\hbar}[\hat{V}(t), \cdot]$. The terms \hat{H}_0 , \hat{K} , and $\hat{V}(t)$ will be defined in the following sections.

2.1.2 The spin Hamiltonian

The Hamiltonian operator determines the coherent evolution of the spins in the radical pair. The total time-dependent Hamiltonian is a sum of two single radical Hamiltonian operators and an electron spin coupling term.^[14]

$$\hat{H}(t) = \hat{H}_1(t) + \hat{H}_2(t) + \hat{H}_{1,2}(t) \quad (2.6)$$

The individual radical components, $\hat{H}_i(t)$, can be expressed as the sum of the Zeeman interaction terms and the electron-nuclear spin coupling terms for the N_i nuclear spins in radical i

$$\hat{H}_i(t) = \mu_B \hat{\mathbf{S}}_i \cdot \mathbf{g}_i(t) \cdot \mathbf{B}_0 + \sum_{k=1}^{N_i} \hat{\mathbf{S}}_i \cdot \mathbf{A}_{i,k}(t) \cdot \hat{\mathbf{I}}_{i,k}. \quad (2.7)$$

Here $\hat{\mathbf{S}}_i$ and $\hat{\mathbf{I}}_{i,k}$ are the unitless electron and nuclear spin operators for radical i and nucleus k , $\mathbf{g}_i(t)$ is the anisotropic g-tensor for radical i and $\mathbf{A}_{i,k}(t)$ is the anisotropic hyperfine coupling tensor between the electron spin and nuclear spin k in the radical. \mathbf{B}_0 is the external magnetic field and μ_B is the Bohr magneton.

The electron spin coupling component $\hat{H}_{1,2}(t)$ is a sum of scalar coupling, $J(t)$, and anisotropic dipolar coupling tensor, $\mathbf{D}(t)$, contributions:

$$\hat{H}_{1,2}(t) = -2J(t)\hat{\mathbf{S}}_1 \cdot \hat{\mathbf{S}}_2 + \hat{\mathbf{S}}_1 \cdot \mathbf{D}(t) \cdot \hat{\mathbf{S}}_2. \quad (2.8)$$

The terms $\mathbf{g}_i(t)$, $\mathbf{A}_{i,k}(t)$, $J(t)$ and $\mathbf{D}(t)$ exhibit time-dependence as they are all mediated by the fluctuating spatial and orientational coordinates of the radical pair nuclear configuration. Various types of spin relaxation arise from these time-dependent fluctuations of spin-coupling terms.

The construction of this Hamiltonian has implicitly made assumptions that other interactions are essentially negligible. These interactions include: the nuclear Zeeman interaction^[16]; nuclear-dipole interactions^[17]; nuclear-orbital interactions^[18]; and nuclear-quadrupolar interactions^[18]. All of these interactions are orders of magnitude smaller than the terms that are included above. This is because the gyromagnetic ratio of a particle is inversely proportional to its mass and therefore the nuclear spins have significantly smaller gyromagnetic ratios than electron spins^[19] [16].

2.1.3 The Zeeman interaction

In a potential which has rotational symmetry, such as an atom, the Zeeman interaction between an electron and a magnetic field is

$$\hat{H}_Z = \mu_B \left(\hat{\mathbf{L}} + g_e \hat{\mathbf{S}} \right) \cdot \mathbf{B} \quad (2.9)$$

where $\hat{\mathbf{L}}$ is defined as the electron orbital angular momentum and g_e as the free electron g-factor. However in a molecule, the electric potential field does not possess rotational symmetry and there are more complex interactions due to spin-orbit coupling. For small organic molecules the spin-orbit coupling is very small and the orbital angular momentum $\hat{\mathbf{L}}$ is suppressed. This leads to a correction to the g-tensor so that the Zeeman contribution is given to a good approximation by

$$\hat{H}_Z = \mu_B \hat{\mathbf{S}} \cdot \mathbf{g}(t) \cdot \mathbf{B} \quad (2.10)$$

where the anisotropic g-tensor has an intrinsic time-dependence due to modulation by rotational motion^[20]. The g-tensor is often determined empirically from EPR spectra, however the values used in this thesis were calculated using DFT^[21].

2.1.4 The hyperfine interaction

The hyperfine interaction couples the unpaired electron spin in each radical with the internal magnetic field generated by the spins of magnetic nuclei. There are two contributions to the hyperfine interaction, the isotropic Fermi contact interaction

and the anisotropic dipolar coupling interaction between the magnetic moments of the unpaired electron and the nuclei^[16]. The dipolar interaction is an interaction of two magnetic moments separated by a finite distance whereas the Fermi contact interaction is the non-vanishing component calculated in the limit of zero separation between the two magnetic moments^[22]. Consequently the anisotropic hyperfine interaction tensor components depend upon the electronic structure of the species. The Fermi contact interaction, which depends upon there being a finite probability density in the distribution for the electron spin at the nucleus, is generally the dominant contribution for the interaction between the electron and hydrogen nuclei. However for the nitrogen nuclei, where the electronic wavefunction vanishes at the nuclear site, the dipolar interaction is dominant^[23].

2.1.5 The Scalar coupling interaction

The scalar electron coupling constant, J , arises from electron correlation terms with contributions from direct exchange and superexchange interactions^[8].

The direct exchange interaction couples two electron spins when they are close enough to have sufficient overlap of their wavefunctions. It gives a strong but short range coupling which decreases rapidly upon separation. This interaction is a consequence of the Pauli principle which states that Fermions must be anti-symmetric with respect to particle exchange. The spin component of the total wavefunction for triplet states is symmetric and thus the spatial component must be anti-symmetric. For anti-symmetric spatial wavefunctions there exists a Fermi hole in the relative distribution of the two electrons because the electrons are formally forbidden from being defined by the same spatial coordinates. Analogously in the singlet state, which must have a symmetric spatial wavefunction, there exists a Fermi heap in the relative distribution. The singlet and triplet states are therefore energetically separated by the direct exchange interaction ($E_T < E_S$) such that the coupling constant, J , must be negative.

The contribution from the superexchange mechanism is a perturbative correction to the exchange term. It originates from the exchange interactions with the overlapping bridging orbitals in a radical pair separated by a molecular wire. The superexchange coupling may contribute a ferromagnetic (stabilising the triplet states) or antiferromagnetic (stabilising the singlet states) component to the overall exchange coupling and therefore J can be positive or negative depending upon the dominant contribution.

2.1.6 The dipolar coupling interaction

Each electron spin interacts with the magnetic field generated by the other unpaired electron spin via the dipolar coupling mechanism which can be reduced to the equation

$$\hat{H}_D = -\left(\frac{\mu_0\gamma_1\gamma_2\hbar^2}{4\pi r_{12}^3}\right) \hat{\mathbf{S}}_1 \cdot \mathbf{D} \cdot \hat{\mathbf{S}}_2 \quad (2.11)$$

where \mathbf{D} is the anisotropic dipolar interaction tensor. This expression is valid for point dipoles which are separated by a vector of length r_{12} . The dipolar interaction causes a lifting of the degeneracy of triplet states at zero field. However, when the molecule is rapidly tumbling in solution, the rotational diffusive motion of one radical around the other results in the interaction averaging to zero.

2.1.7 The Haberkorn recombination operator

The Haberkorn recombination operator was initially proposed phenomenologically, however recently it has been derived from non-adiabatic reaction rate theory using the Nakajima-Zwanzig formalism and second order perturbation theory^[24]. This operator accounts for the spin selective electron transfer reactions of the radical pair and is given by

$$\hat{K} = \frac{k_S}{2}\hat{P}_S + \frac{k_T}{2}\hat{P}_T \quad (2.12)$$

where k_S and k_T are the first order singlet and triplet recombination rates and \hat{P}_S and \hat{P}_T are the singlet and triplet projection operators respectively. The projection

operators are defined by

$$\hat{P}_S = |S\rangle \langle S| = \frac{1}{4} \hat{\mathbf{1}} - \hat{\mathbf{S}}_1 \cdot \hat{\mathbf{S}}_2 \quad (2.13)$$

$$\hat{P}_T = |T_+\rangle \langle T_+| + |T_0\rangle \langle T_0| + |T_-\rangle \langle T_-| = \frac{3}{4} \hat{\mathbf{1}} + \hat{\mathbf{S}}_1 \cdot \hat{\mathbf{S}}_2 \quad (2.14)$$

with $\hat{\mathbf{1}}$ being the unit operator^[25].

This reaction operator gives the desired dynamics in the two limiting cases of symmetric recombination ($k_S = k_T$) and in the absence of other terms which influence the evolution of the spin dynamics ($\hat{H} = 0$)^[25]. Furthermore the Haberkorn operator obeys the exact sum rule for the product quantum yields $\phi_S + \phi_T = 1$ ^[13] and, in the quantum master equation, it acts to preserve the purity of the states^[26].

2.2 Semi-classical methods.

2.2.1 Schulten-Wolynes approximation

Schulten and Wolynes introduced a static nuclear spin bath approximation for modelling the dynamics of radical pairs^[27]. This method can provide an accurate approximation to the spin dynamics of a system of short lived radical pairs or for systems where the electron-nuclear spin interaction terms are much smaller than the electron-electron spin interaction terms. This is particularly useful in molecules with many nuclear spins, as is common in real organic radical pairs, due to the computational expense of fully quantum mechanical simulations. In the static bath approximation the nuclear spin operators $\hat{I}_{i,k}$ are replaced by classical vectors of length $\sqrt{I_{i,k}(I_{i,k} + 1)}$ which are sampled from the surface of a sphere^[13]. The reduced density operator of the electron spin subsystem is then calculated using Monte-Carlo sampling over orientations of the nuclear spins. This effectively averages over all possible realisations of the nuclear spin vectors. The number of nuclear spins should be sufficiently large so that the hyperfine-weighted resultant vector of all the nuclear spins,

$$\mathbf{I}_i = \sum_{k=1}^{N_i} a_{ik} \mathbf{I}_{ik} \quad (2.15)$$

is approximately constant. This method becomes exact in the limit $N \rightarrow \infty$ provided all the individual hyperfine coupling constants a_{ik} decay to zero in this limit. However, the approximation is not consistent with Newton's third law of motion as the force acted upon the nuclear spins by the electron spin is not accounted for in the model.

With the Schulten-Wolynes approximation the trace of the reduced density operator is approximated by the average of the integral over all possible orientations of nuclear spins,

$$\frac{1}{Z} \text{Tr}_{\text{nuc}} [\hat{\rho}(t)] \approx \int \hat{\rho}_{SW}(t, \mathbf{I}) d\mathbf{I} \approx \left(\frac{1}{4\pi} \right)^{N_1+N_2} \int \hat{\rho}_{SW}(t, \boldsymbol{\Omega}_{1,1}, \dots, \boldsymbol{\Omega}_{2,N_2}) d\boldsymbol{\Omega}_{1,1} \dots d\boldsymbol{\Omega}_{2,N_2} \quad (2.16)$$

where \mathbf{I} represents the set of nuclear spin vectors and $\hat{\rho}_{SW}(t, \mathbf{I})$ represents the reduced density matrix for a given representation of the static bath at time t . The normalisation term, $Z = \prod_{i=1}^2 \prod_{k=1}^{N_i} (2I_{ik} + 1)$, is the total number of nuclear spin states in the radical pair.

The vector $\boldsymbol{\Omega}_{i,k}(\theta, \phi)$ represents the classical orientation of the nuclear spin I_{ik} which interacts with electron i and is a function of its spherical polar angles, θ and ϕ . The nuclear spin operators in the master equation also need to be replaced by their classical analogues in order to calculate the dynamics.

2.2.2 Redfield Theory

Electron spins relax to equilibrium due to modulation by time dependent fluctuations in magnetic interactions in the radical pair. These fluctuations arise from molecular motions and as such are very complex to model via explicit quantum mechanical methods. Redfield theory is a perturbative method for describing the dynamics of the density matrix of a system in contact with a thermal bath and therefore can be used to describe spin relaxation processes^[28]. The core principles and assumptions of Redfield theory, as well as its implementation with respect to the system of interest in this thesis, are outlined in the following discussion.

The time-dependent system Hamiltonian is defined by

$$\hat{H}(t) = \hat{H}_0 + \hat{V}(t) \quad (2.17)$$

where $\hat{H}_0 = \langle \hat{H}(t) \rangle$ is a time independent component of \hat{H} and $\hat{V}(t) = \hat{H}(t) - \langle \hat{H}(t) \rangle$ is a time-dependent fluctuation term. $\hat{V}(t)$ is defined such that the thermally averaged time dependent fluctuations of the Hamiltonian operator are zero ($\langle \hat{V}(t) \rangle = 0$).

The dynamics of the time dependent density matrix are given by the the Stochastic Liouville-von Neumann equation,

$$\frac{d\hat{\rho}(t)}{dt} = \mathcal{L}(t)\hat{\rho}(t), \quad (2.18)$$

where the Liouvillian Superoperator $\mathcal{L}(t)$ can be split into time-dependent and time-independent components, $\mathcal{L}(t) = \mathcal{L}_0 + \mathcal{L}_V(t)$. It is convenient to continue the derivation in the interaction picture using the relation

$$\hat{\rho}^I(t) = e^{-\mathcal{L}_0 t} \hat{\rho}(t). \quad (2.19)$$

The derivative of the interaction picture density matrix with respect to time is found to be

$$\frac{d\hat{\rho}^I(t)}{dt} = -\mathcal{L}_0 e^{-\mathcal{L}_0 t} \hat{\rho}(t) + e^{-\mathcal{L}_0 t} \left(\frac{d(\hat{\rho}(t))}{dt} \right) = -\mathcal{L}_0 \hat{\rho}^I(t) + e^{-\mathcal{L}_0 t} \mathcal{L}(t) \hat{\rho}(t) \quad (2.20)$$

$$\frac{d\hat{\rho}^I(t)}{dt} = -\mathcal{L}_0 \hat{\rho}^I(t) + e^{-\mathcal{L}_0 t} \left(\mathcal{L}_0 + \mathcal{L}_V(t) \right) e^{+\mathcal{L}_0 t} e^{-\mathcal{L}_0 t} \hat{\rho}(t) \quad (2.21)$$

where, after separating the Liouvillian into its time dependent and time independent terms, the identity operator $e^{+\mathcal{L}_0 t} e^{-\mathcal{L}_0 t}$, is inserted so as to replace the general density operator $\hat{\rho}(t)$ by the interaction picture density operator $\hat{\rho}^I(t)$,

$$\frac{d\hat{\rho}^I(t)}{dt} = -\mathcal{L}_0 \hat{\rho}^I(t) + e^{-\mathcal{L}_0 t} \mathcal{L}_0 e^{+\mathcal{L}_0 t} \hat{\rho}^I(t) + e^{-\mathcal{L}_0 t} \mathcal{L}_V(t) e^{+\mathcal{L}_0 t} \hat{\rho}^I(t). \quad (2.22)$$

All terms containing only \mathcal{L}_0 commute and thus the first two terms cancel, giving

$$\frac{d\hat{\rho}^I(t)}{dt} = (e^{-\mathcal{L}_0 t} \mathcal{L}_V(t) e^{+\mathcal{L}_0 t}) \hat{\rho}^I(t). \quad (2.23)$$

Here we can define the interaction picture Liouvillian superoperator,

$$\mathcal{L}_V^I(t) = e^{-\mathcal{L}_0 t} \mathcal{L}_V(t) e^{+\mathcal{L}_0 t} \quad (2.24)$$

and express the dynamics of the density matrix in the interaction picture as

$$\frac{d\hat{\rho}^I(t)}{dt} = \mathcal{L}_V^I(t)\hat{\rho}^I(t). \quad (2.25)$$

Formally integrating this equation and then applying the interaction picture superoperator gives the expansion series

$$\int_0^t \left(\frac{d\hat{\rho}^I(\tau)}{d\tau} \right) d\tau = \int_0^t (\mathcal{L}_V^I(\tau)\hat{\rho}^I(\tau)) d\tau \quad (2.26)$$

$$\hat{\rho}^I(t) - \hat{\rho}^I(0) = \int_0^t \mathcal{L}_V^I(\tau)\hat{\rho}^I(\tau) d\tau \quad (2.27)$$

$$\mathcal{L}_V^I(t)\hat{\rho}^I(t) = \mathcal{L}_V^I(t)\hat{\rho}^I(0) + \int_0^t \mathcal{L}_V^I(t)\mathcal{L}_V^I(\tau)\hat{\rho}^I(\tau) d\tau \quad (2.28)$$

$$\frac{d\hat{\rho}^I(t)}{dt} = \mathcal{L}_V^I(t)\hat{\rho}^I(0) + \int_0^t \mathcal{L}_V^I(t)\mathcal{L}_V^I(\tau)\hat{\rho}^I(\tau) d\tau. \quad (2.29)$$

Given that \mathcal{L}_0 is defined as a thermally averaged superoperator, and $\langle \hat{\rho}(t) \rangle = e^{\mathcal{L}_0 t} \langle \hat{\rho}^I(t) \rangle$, the ensemble average for the dynamics of the interaction picture density operator can be written

$$\frac{d}{dt} \langle \hat{\rho}(t) \rangle = \langle \mathcal{L}_V^I(t)\hat{\rho}^I(0) \rangle + \int_0^t \langle \mathcal{L}_V^I(t)\mathcal{L}_V^I(\tau)\hat{\rho}^I(\tau) \rangle d\tau \quad (2.30)$$

where by definition

$$\langle \mathcal{L}_V^I(t) \rangle = -(i/\hbar) \left[\langle \hat{V}^I(t) \rangle, \cdot \right] = 0 \quad (2.31)$$

such that the final result is given by

$$\frac{d}{dt} \langle \hat{\rho}(t) \rangle = \int_0^t \langle \mathcal{L}_V^I(t)\mathcal{L}_V^I(\tau)\hat{\rho}^I(\tau) \rangle d\tau. \quad (2.32)$$

This equation is exact as no approximations have been made, but it is just as difficult to solve as the full stochastic Liouville equation. If we now introduce the approximation that all fluctuations in $\hat{V}(t)$ are uncorrelated with $\hat{\rho}^I(t)$ the integrand can be approximated as

$$\langle \mathcal{L}_V^I(t)\mathcal{L}_V^I(\tau)\hat{\rho}^I(\tau) \rangle \approx \langle \mathcal{L}_V^I(t)\mathcal{L}_V^I(\tau) \rangle \langle \hat{\rho}^I(\tau) \rangle. \quad (2.33)$$

The time-dependent Liouvillian $\mathcal{L}_V(t)$ can be expressed as a combination of Liouville superoperators \mathcal{A}_k and time-dependent fluctuation terms $f_k(t)$,

$$\mathcal{L}_V(t) = \sum_k \mathcal{A}_k f_k(t) \quad (2.34)$$

where, $\mathcal{A}_k = -(i/\hbar) \left[\hat{A}_k, \cdot \right]$, so that the correlation function can be expressed as

the sum

$$\langle \mathcal{L}_V^I(t) \mathcal{L}_V^I(\tau) \rangle = \sum_{i,k} \langle e^{-\mathcal{L}_0 t} \left(\mathcal{A}_k f_k(t) \right) e^{+\mathcal{L}_0 t} e^{-\mathcal{L}_0 \tau} \left(\mathcal{A}_j^\dagger f_j^*(\tau) \right) e^{+\mathcal{L}_0 \tau} \rangle \quad (2.35)$$

The correlation function is observed to only depend upon the difference between the two time frames and therefore depends upon a single variable, so that it is given by

$$\langle f_k(t) f_j^*(\tau) \rangle \equiv g_{k,j}(t, \tau) = g_{k,j}(|t - \tau|). \quad (2.36)$$

Generally, the terms $g_{k,j}(|t - \tau|)$ decay on a much faster timescale than the evolution of the density operator $\langle \hat{\rho}^I(\tau) \rangle$ and as such $\langle \hat{\rho}^I(\tau) \rangle$ can be replaced by $\langle \hat{\rho}^I(t) \rangle$. The resulting equation is valid to the same order in the perturbative expansion as the first approximation and is therefore Markovian. This argument essentially assumes that there are no memory effects, so that the system's effect on the bath is instantaneously 'forgotten'.

The ensemble averaged time-dependent Master equation can now be written in terms of the Redfield superoperator $\mathcal{R}(t)$,

$$\frac{d}{dt} \langle \hat{\rho}(t) \rangle = \mathcal{L}_0 \langle \hat{\rho}(t) \rangle + \mathcal{R}(t) \langle \hat{\rho}(t) \rangle, \quad (2.37)$$

where

$$\mathcal{R}(t) = \int_0^t d\tau \langle \mathcal{L}_V^I(t) \mathcal{L}_V^I(\tau) \rangle \quad (2.38)$$

such that, after cyclically permuting the inner product and using the summation of the correlation terms,

$$\mathcal{R}(t) = \int_0^t d\tau \langle \mathcal{L}_V(t) e^{+\mathcal{L}_0(t-\tau)} \mathcal{L}_V(\tau) e^{-\mathcal{L}_0(t-\tau)} \rangle \quad (2.39)$$

$$\mathcal{R}(t) = - \sum_{j,k} \int_0^t d\tau g_{j,k}(t - \tau) \mathcal{A}_j^\dagger e^{+\mathcal{L}_0(t-\tau)} \mathcal{A}_k e^{-\mathcal{L}_0(t-\tau)}. \quad (2.40)$$

If the correlation functions decay on a much shorter timescale than evolution of the density operator then it is valid to replace the upper limit t of the integral over τ in Eq. (2.40) with $t \rightarrow \infty$, giving $\mathcal{R}(t) \rightarrow \mathcal{R}(t \rightarrow \infty) = \mathcal{R}$. By replacing $(t - \tau)$ with

(τ) and taking the limit ($t \rightarrow \infty$) the Redfield superoperator can be written as

$$\mathcal{R} = - \sum_{j,k} \int_0^\infty d\tau g_{j,k}(\tau) \mathcal{A}_j^\dagger e^{+\mathcal{L}_0\tau} \mathcal{A}_k e^{-\mathcal{L}_0\tau} \quad (2.41)$$

$$\mathcal{R} = - \sum_{j,k} \int_0^\infty d\tau g_{j,k}(\tau) \mathcal{A}_j^\dagger \mathcal{A}_k^I(\tau) \quad (2.42)$$

This derivation is valid in the case of where $e^{\mathcal{L}_0 t}$ is a non-unitary evolution operator in the case of asymmetric radical pair recombination ($k_S \neq k_T$). Finally treating the fluctuations of the system bath interactions stochastically and using Schulten-Wolynes approximation, the time-dependent reduced density operator for the spin system can be written with the standard Hamiltonian replaced by its classical counterpart,

$$\frac{d\hat{\rho}_{SW}(t, \mathbf{I})}{dt} = -i[\hat{\mathbf{H}}_{SW}(t, \mathbf{I}), \hat{\rho}_{SW}(t, \mathbf{I})] - \{\hat{\mathbf{K}}, \hat{\rho}_{SW}(t, \mathbf{I})\}. \quad (2.43)$$

The Redfield approximation can be applied to this master equation as before,

$$\frac{d\langle \hat{\rho}_{SW}(t, \mathbf{I}) \rangle}{dt} = -i[\hat{\mathbf{H}}_{0,SW}(\mathbf{I}), \langle \hat{\rho}_{SW}(t, \mathbf{I}) \rangle] - \{\hat{\mathbf{K}}, \langle \hat{\rho}_{SW}(t, \mathbf{I}) \rangle\} - \mathcal{R}_{SW}(\mathbf{I}) \langle \hat{\rho}_{SW}(t, \mathbf{I}) \rangle. \quad (2.44)$$

Chapter 3

Implementation

In this chapter the methods for implementing Redfield theory, as well as the extreme narrowing limit method are discussed for asymmetric recombination of a radical pair under the static bath approximation.

3.1 Liouville Space

3.1.1 Hilbert space

The solutions to the Schrödinger equation, termed wavefunctions, have properties such that they can be represented by complex vectors which are defined as Dirac kets $|\phi_i\rangle$. Dirac bras are defined as the complex conjugate of Dirac kets and represented by $\langle\phi_i| \equiv |\phi_i\rangle^\dagger$. This state space is defined as a Hilbert space because it is a linear vector space with a metric which in this instance is the inner product. It will now be assumed that the kets form a complete orthonormal basis set $|i\rangle$ so that any wavefunction can be represented as a linear combination of the basis set. This vector space is commonly referred to as the quantum mechanical “Hilbert Space” although it is only a specific instance of such a space. The operators in this “Hilbert Space” form a vector space termed Liouville space where each Liouville space ket is defined by a “Hilbert space” operator $|i\rangle\langle j| = |i, j\rangle$.

3.1.2 Bras and Kets

Since the Liouville ket has been defined as an operator of a complete orthonormal basis set, it follows that the Liouville kets and their duals, bras, should also form a complete orthonormal set so that $\left(i, j \middle| k, l\right) = \delta_{i,k} \delta_{j,l}$.

To satisfy this requirement the Liouville bras are defined, using the quantum

mechanical trace, by

$$\left(|i, j\rangle \equiv |i, j\rangle \right)^\dagger \equiv \text{Tr} \left[(|i\rangle \langle j|)^\dagger \cdot \right] \equiv \text{Tr} \left[|j\rangle \langle i| \cdot \right]. \quad (3.1)$$

The Liouville bras and kets now form a complete orthonormal basis set in a linear vector space and can be used to define operators within this space.

3.1.3 Superoperators

The operators within Liouville space are termed superoperators because, within “Hilbert Space”, they operate on standard operators. Superoperators can be expanded in terms of “Hilbert Space” bras and kets to give an equation for the action of a superoperator in “Hilbert Space”,

$$|i, j\rangle \left(|l, k\rangle \cdot \right) = \left\{ |i\rangle \langle j| \right\} \text{Tr} \left[|k\rangle \langle l| \cdot \right] \quad (3.2)$$

$$= \left\{ |i\rangle \langle j| \right\} \langle l| \cdot |k\rangle \quad (3.3)$$

$$= |i\rangle \langle l| \cdot |k\rangle \langle j| \quad (3.4)$$

3.1.4 Matrix representation

It is much more efficient to evaluate quantum mechanical expressions computationally using matrix-vector linear algebra. A state $|\psi\rangle$ can be expanded as a linear combination of the orthonormal basis set of kets given by $|\psi\rangle = \psi_i |i\rangle$ where the expansion coefficients, given by $\psi_i = \langle i | \psi \rangle$ can be expressed as a column vector

$$\boldsymbol{\psi} = \begin{pmatrix} \psi_1 \\ \cdot \\ \cdot \\ \cdot \\ \psi_n \end{pmatrix}. \quad (3.5)$$

Analogously an operator $\hat{\Omega} = \sum_{i,j} \Omega_{ij} |i\rangle \langle j|$ can be defined in terms of a matrix with matrix elements $\Omega_{ij} = \langle i | \hat{\Omega} | j \rangle$. A new state $\boldsymbol{\chi}$ can be derived from the action of an operator on a vector state $\boldsymbol{\psi}$ as follows,

$$|\chi\rangle = \hat{\Omega} |\psi\rangle = \sum_{i,j,k} \Omega_{ij} |i\rangle \langle j| \psi_k |k\rangle. \quad (3.6)$$

Due to the orthonormality condition this equation reduces to $|\chi\rangle = \sum_i \left(\sum_j \Omega_{ij} \psi_j \right) |i\rangle$ so that the new state may be expanded into a vector form in terms of the basis set $i = 1, \dots, n$,

$$\chi = \begin{pmatrix} \sum_j \Omega_{1j} \psi_j \\ \vdots \\ \sum_j \Omega_{nj} \psi_j \end{pmatrix} \quad (3.7)$$

Hence the action of the operator on a “Hilbert Space” state vector is equivalent to a matrix-vector multiplication so that the operator in matrix form is given by

$$\Omega = \begin{pmatrix} \Omega_{11} & \Omega_{12} & \cdot & \cdot \\ \Omega_{21} & \Omega_{22} & \cdot & \cdot \\ \cdot & \cdot & \cdot & \cdot \\ \cdot & \cdot & \cdot & \Omega_{nn} \end{pmatrix}. \quad (3.8)$$

Equivalently, Liouville space states can be expressed as column vectors by the reduction of the sum over two variables $|\Omega\rangle = \sum_{ij} \Omega_{ij} |i\rangle \langle j| = \sum_{ij} \Omega_{ij} |i, j\rangle$ to a sum over a single variable $|\Omega\rangle = \sum_a \Omega_a |a\rangle$ which can then be written in column vector form as before. The action of an operator on a Liouville space state to produce another state is again equivalent to a matrix-vector multiplication so that these superoperators are written as matrices in Liouville space. Expanding a Liouville superoperator \mathcal{A} in terms of “Hilbert Space” operators gives

$$\mathcal{A} = \sum_{a,b,c,d} A_{(ab),(cd)} |a, b\rangle \langle c, d| = \sum_{a,b,c,d} A_{(ab),(cd)} |a\rangle \langle c| \cdot [|b\rangle \langle d|]^\dagger. \quad (3.9)$$

If $A_{(ab),(cd)}$ can be factorised this equation becomes

$$\mathcal{A} = \left[\sum_{a,c} X_{(ac)} |a\rangle \langle c| \right] \cdot \left[\sum_{b,d} Y_{(bd)} |b\rangle \langle d| \right]^T = \hat{X} \cdot \hat{Y}^\dagger \quad (3.10)$$

where \hat{X} and \hat{Y} are operators in “Hilbert Space”. In this case the superoperator matrix elements $A_{(ab),(cd)} = X_{(ac)}(Y_{(bd)})^*$ can be formed from a Krønecker product of the “Hilbert Space” operator matrices using the mapping scheme

$$\hat{X} \cdot \hat{Y} \iff \mathcal{A} = \mathbf{X} \otimes \mathbf{Y}^T. \quad (3.11)$$

In this way the quantum master equation can be reformulated in terms of superoperator matrices and density operator vectors.

3.2 Monte-Carlo sampling

In the static bath approximation the nuclear spin operators $\hat{I}_{i,k}$ are replaced by classical vectors of length $\sqrt{I_{i,k}(I_{i,k} + 1)}$ which are stochastically sampled from the surface of a sphere. Properties are calculated as the average property over all orientations which is equivalent to approximating an integral with a sum, given by

$$\left(\frac{1}{4\pi}\right)^{N_1+N_2} \int \hat{\rho}_{SW}(t, \boldsymbol{\Omega}_{1,1}, \dots, \boldsymbol{\Omega}_{2,N_2}) d\boldsymbol{\Omega}_{1,1} \dots d\boldsymbol{\Omega}_{2,N_2} \quad (3.12)$$

$$\approx \frac{1}{N} \sum_{\alpha=1}^N \hat{\rho}_{SW}(t, \boldsymbol{\Omega}_{1,1(\alpha)} \dots \boldsymbol{\Omega}_{2,n_2(\alpha)}) \quad (3.13)$$

where $\boldsymbol{\Omega}_{i,k(\alpha)}$ represents the orientation of the classical vector for the nuclear spin \mathbf{I}_{ik} in radical i . Each vector is defined by its vector length \mathbf{I} and the angles $\theta_{i,k(\alpha)}$ and $\phi_{i,k(\alpha)}$ where each value α represents a single instance of a vector sampled from a uniform distribution over the surface of a sphere. Figure 3.1 shows the convergence of the radical pair lifetimes at different field strengths as the number N of sampled orientations increases.

3.2.1 Sampling from the surface of a sphere

When stochastically sampling points on the surface of a unit sphere it is incorrect to sample θ and ϕ from uniform distributions because the area element $d\Omega = \sin(\theta)d\theta d\phi$ is a function of θ and thus the points would be concentrated around the poles. Instead the correct procedure is to define the angles, ϕ and θ , as

$$\phi_i = \arccos(2 \times u_i - 1) \quad (3.14)$$

$$\theta_i = 2\pi \times v_i \quad (3.15)$$

where u_i and v_i are independent random variables^[29]. This approach gives the coordinates of a distribution which is uniform over the surface of the unit sphere. Therefore, the Cartesian coordinates of vectors sampled uniformly from the surface

of a sphere are,

$$I_x = I \times \cos(\theta) \times \sin(\phi) \quad (3.16)$$

$$I_y = I \times \sin(\theta) \times \sin(\phi) \quad (3.17)$$

$$I_z = I \times \cos(\phi) \quad (3.18)$$

where I is the length of a nuclear spin vector.

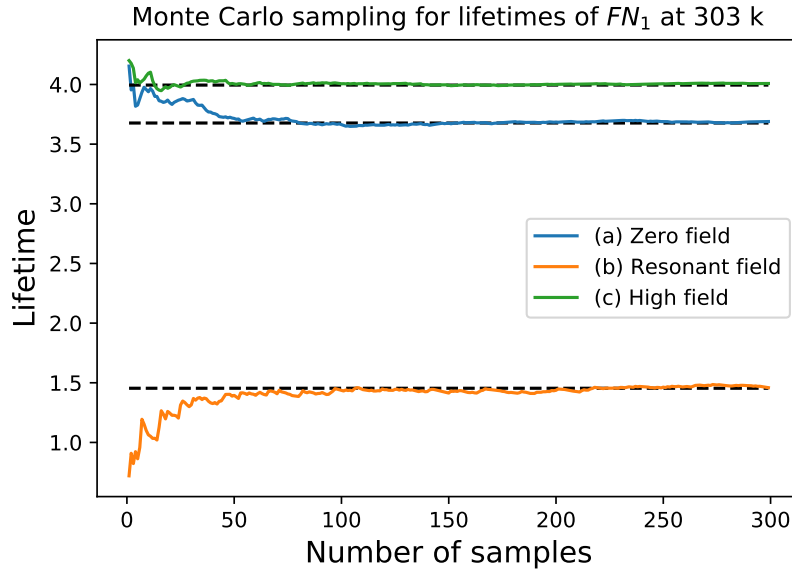


Figure 3.1: Convergence of Monte-Carlo sampling for the lifetimes.

3.3 Matrix representation of Redfield theory

For a reference Liouville superoperator \mathcal{L}_0 which does preserve pure states the expression is evaluated by using the relation $e^{\mathcal{L}_0 t} \hat{O} = e^{-i\hat{\Omega} t} \hat{O} e^{+i\hat{\Omega}^\dagger t}$ where \hat{O} is an operator in “Hilbert Space” and by definition for the problem we are interested in $\hat{\Omega} = (\hat{H}_0/\hbar) - i\hat{K}$. Acting the Redfield superoperator, from equation 2.41, on an operator \hat{O} gives

$$\mathcal{R}\hat{O} = - \sum_{j,k} \int_0^t d\tau g_{j,k}(\tau) \mathcal{A}_j^\dagger e^{\mathcal{L}_0 \tau} \mathcal{A}_k e^{-\mathcal{L}_0 \tau} \hat{O} \quad (3.19)$$

$$\mathcal{R}\hat{O} = - \sum_{j,k} \int_0^t d\tau g_{j,k}(\tau) \mathcal{A}_j^\dagger e^{\mathcal{L}_0 \tau} \mathcal{A}_k (e^{+i\hat{\Omega} \tau} \hat{O} e^{-i\hat{\Omega}^\dagger \tau}). \quad (3.20)$$

The Liouville superoperator is defined in terms of the ‘‘Hilbert Space’’ operators by $\mathcal{A}_k = -i[\hat{A}_k, \cdot]$. Using this definition, equation 3.20 can be expanded to give

$$\mathcal{R}\hat{O} = i \sum_{j,k} \int_0^\infty d\tau g_{j,k}(\tau) \mathcal{A}_j^\dagger e^{\mathcal{L}_0\tau} [\hat{A}_k, e^{+i\hat{\Omega}\tau} \hat{O} e^{-i\hat{\Omega}^\dagger\tau}] \quad (3.21)$$

$$\mathcal{R}\hat{O} = i \sum_{j,k} \int_0^\infty d\tau g_{j,k}(\tau) \mathcal{A}_j^\dagger \left(e^{-i\hat{\Omega}\tau} (\hat{A}_k e^{+i\hat{\Omega}\tau} \hat{O} e^{-i\hat{\Omega}^\dagger\tau} - e^{+i\hat{\Omega}\tau} \hat{O} e^{-i\hat{\Omega}^\dagger\tau} \hat{A}_k) e^{-i\hat{\Omega}^\dagger\tau} \right) \quad (3.22)$$

$$\mathcal{R}\hat{O} = -i^2 \sum_{j,k} \int_0^\infty d\tau g_{j,k}(\tau) [\hat{A}_j^\dagger, e^{-i\hat{\Omega}\tau} \hat{A}_k e^{+i\hat{\Omega}\tau} \hat{O} - \hat{O} e^{-i\hat{\Omega}^\dagger\tau} \hat{A}_k e^{-i\hat{\Omega}^\dagger\tau}]. \quad (3.23)$$

3.3.1 Linear algebra

The ensemble average of an operator $\langle \hat{O}(\tau) \rangle$ can be written as a vector $\hat{\mathbf{O}}(\tau)$ and thus the superoperators can be expressed matrices. The action of general superoperator $\hat{A} \langle \hat{O}(\tau) \rangle \hat{B}$ can be written as the matrix vector operation $\hat{A} \langle \hat{O}(\tau) \rangle \hat{B} \leftrightarrow (\mathbf{A} \otimes \mathbf{B}^T) \hat{\mathbf{O}}(\tau)$. By defining the Redfield superoperator, in matrix form, in terms of components $\mathcal{M}_{j,k}$, we have $\mathcal{R} = -\sum_{j,k} \int_0^\infty d\tau g_{j,k}(\tau) \mathcal{M}_{j,k}$. If $\mathbf{1}$ is the identity operator matrix and as before, \otimes is the Kronecker product of the matrices, then equation 3.23 can be fully expanded to give the components

$$\mathcal{M}_{j,k} \hat{\mathbf{O}} = \hat{\mathbf{A}}_j^\dagger e^{-i\hat{\Omega}\tau} \hat{\mathbf{A}}_k e^{+i\hat{\Omega}\tau} \hat{\mathbf{O}} \mathbf{1} - \hat{\mathbf{A}}_j^\dagger \hat{\mathbf{O}} e^{-i\hat{\Omega}^\dagger\tau} \hat{\mathbf{A}}_k e^{-i\hat{\Omega}^\dagger\tau} \quad (3.24)$$

$$- e^{-i\hat{\Omega}\tau} \hat{\mathbf{A}}_k e^{+i\hat{\Omega}\tau} \hat{\mathbf{O}} \hat{\mathbf{A}}_j^\dagger + \mathbf{1} \hat{\mathbf{O}} e^{-i\hat{\Omega}^\dagger\tau} \hat{\mathbf{A}}_k e^{-i\hat{\Omega}^\dagger\tau} \hat{\mathbf{A}}_j^\dagger \quad (3.25)$$

$$= \left((\hat{\mathbf{A}}_j^\dagger e^{-i\hat{\Omega}t} \hat{\mathbf{A}}_k e^{+i\hat{\Omega}t}) \otimes (\mathbf{1})^T \right. \quad (3.26)$$

$$\left. - (\hat{\mathbf{A}}_j^\dagger) \otimes (e^{-i\hat{\Omega}^\dagger t} \hat{\mathbf{A}}_k e^{-i\hat{\Omega}^\dagger\tau})^T \right) \quad (3.27)$$

$$- (e^{-i\hat{\Omega}t} \hat{\mathbf{A}}_k e^{+i\hat{\Omega}t}) \otimes (\hat{\mathbf{A}}_j^\dagger)^T \quad (3.28)$$

$$+ (\mathbf{1}) \otimes (e^{-i\hat{\Omega}^\dagger\tau} \hat{\mathbf{A}}_k e^{-i\hat{\Omega}^\dagger\tau} \hat{\mathbf{A}}_j^\dagger)^T \hat{\mathbf{O}}. \quad (3.29)$$

In what follows it is assumed that $\hat{\Omega}$, and by extension also $\hat{\Omega}^\dagger$, can be diagonalised such that ω is the diagonal matrix of eigenvalues and $\hat{\Omega} = \mathbf{P}\omega\mathbf{P}^{-1}$.

3.3.2 The spectral density function

The spectral density function, defined as the one sided Fourier transform of the correlation function $g_{j,k}(\tau)$ is given by

$$J_{j,k}(z) = \int_0^\infty g_{j,k}(\tau) e^{iz\tau} d\tau. \quad (3.30)$$

The Redfield superoperator can expressed by the equation

$$\mathcal{R} = - \sum_{j,k} [(\hat{\mathbf{A}}_j^\dagger \mathbf{B}_{j,k}) \otimes (\mathbf{1})^T - \hat{\mathbf{A}}_j^\dagger \otimes (\mathbf{C}_{j,k}^\dagger)^T - \mathbf{B}_{j,k} \otimes (\hat{\mathbf{A}}_j^\dagger)^T + \mathbf{1} \otimes (\mathbf{C}_{j,k}^\dagger \hat{\mathbf{A}}_j^\dagger)^T] \quad (3.31)$$

where $\mathbf{B}_{j,k} = \int_0^\infty d\tau g_{j,k}(\tau) e^{-i\hat{\Omega}\tau} \hat{\mathbf{A}}_k e^{+i\hat{\Omega}\tau}$. Using the eigenvalues and eigenvectors of $\hat{\Omega}$ this component can be rewritten and manipulated as follows,

$$\mathbf{B}_{j,k} = \int_0^\infty d\tau g_{j,k}(\tau) \mathbf{P} e^{-i\boldsymbol{\omega}\tau} \mathbf{P}^{-1} \hat{\mathbf{A}}_k \mathbf{P} e^{i\boldsymbol{\omega}\tau} \mathbf{P}^{-1} \quad (3.32)$$

$$\mathbf{B}_{j,k} = \mathbf{P} \left(\sum_{a,b} \left[\int_0^\infty d\tau g_{j,k}(\tau) e^{-i\boldsymbol{\omega}\tau} \mathbf{P}^{-1} \hat{\mathbf{A}}_k \mathbf{P} e^{i\boldsymbol{\omega}\tau} \right]_{a,b} \right) \mathbf{P}^{-1} \quad (3.33)$$

$$\mathbf{B}_{j,k} = \mathbf{P} \left(\sum_{a,c} \left[\int_0^\infty d\tau g_{j,k}(\tau) e^{-i\boldsymbol{\omega}_{a,c}\tau} \right] \sum_{c,d} \left[\mathbf{P}^{-1} \hat{\mathbf{A}}_k \mathbf{P} \right]_{c,d} \sum_{d,b} \left[e^{i\boldsymbol{\omega}_{d,b}\tau} \right] \right) \mathbf{P}^{-1} \quad (3.34)$$

However only diagonal elements of $\boldsymbol{\omega}$ are non-zero and as such the equation can be reduced to a sum over two variables,

$$\mathbf{B}_{j,k} = \mathbf{P} \left(\sum_a \left[\int_0^\infty d\tau g_{j,k}(\tau) e^{-i\boldsymbol{\omega}_a\tau} \right] \sum_{a,b} \left[\mathbf{P}^{-1} \hat{\mathbf{A}}_k \mathbf{P} \right]_{a,b} \sum_b \left[e^{i\boldsymbol{\omega}_b\tau} \right] \right) \mathbf{P}^{-1} \quad (3.35)$$

$$\mathbf{B}_{j,k} = \mathbf{P} \left(\sum_{a,b} \left[\int_0^\infty d\tau g_{j,k}(\tau) e^{i(\boldsymbol{\omega}_b - \boldsymbol{\omega}_a)\tau} \right] \left[\mathbf{P}^{-1} \hat{\mathbf{A}}_k \mathbf{P} \right]_{a,b} \right) \mathbf{P}^{-1} \quad (3.36)$$

Using the definition of the spectral density functions this equation becomes

$$\mathbf{B}_{j,k} = \mathbf{P} \left(\sum_{a,b} J_{j,k}(\boldsymbol{\omega}_b - \boldsymbol{\omega}_a) \left[\mathbf{P}^{-1} \hat{\mathbf{A}}_k \mathbf{P} \right]_{a,b} \right) \mathbf{P}^{-1} \quad (3.37)$$

$$\mathbf{B}_{j,k} = \mathbf{P} (\mathbf{J}_{j,k} \circ (\mathbf{P}^{-1} \hat{\mathbf{A}}_k \mathbf{P})) \mathbf{P}^{-1} \quad (3.38)$$

where \circ is the element wise product. Similarly the other component, $\mathbf{C}_{j,k}^\dagger$, can be evaluated as

$$\mathbf{C}_{j,k}^\dagger = \int_0^\infty d\tau g_{j,k}(\tau) e^{-i\hat{\Omega}^\dagger\tau} \hat{\mathbf{A}}_k e^{+i\hat{\Omega}^\dagger\tau} = (\mathbf{P} (\mathbf{J}_{j,k} \circ (\mathbf{P}^{-1} \hat{\mathbf{A}}_k^\dagger \mathbf{P})) \mathbf{P}^{-1})^\dagger. \quad (3.39)$$

3.3.3 Observables

The triplet yield can now be evaluated using the superoperator matrices which have been defined in addition to the equation for the evolution of the density matrix

$$\hat{\rho}(t) = e^{(\mathcal{L}_0 + \mathcal{R})t} \hat{\rho}_0. \quad (3.40)$$

By substituting this equation into the formula for the evaluation of an observable, an expression for the triplet yield can be derived in terms of the superoperator matrices acting upon a vector representing the density matrix at time $t = 0$ in Liouville space,

$$\Phi_T = k_T \int_0^\infty dt \operatorname{Tr} [\hat{\mathbf{P}}_T \hat{\rho}(t)] \quad (3.41)$$

$$\Phi_T = k_T \int_0^\infty dt \operatorname{Tr} [\hat{\mathbf{P}}_T e^{(\mathcal{L}_0 + \mathcal{R})t} \hat{\rho}_0] \quad (3.42)$$

$$\Phi_T = k_T \times \operatorname{Tr} \left[\int_0^\infty dt \mathbf{P}_T e^{(\mathcal{L}_0 + \mathcal{R})t} \rho_0 \right] \quad (3.43)$$

$$\Phi_T = k_T \times \operatorname{Tr} \left[[\mathbf{P}_T (\mathcal{L}_0 + \mathcal{R})^{-1} e^{(\mathcal{L}_0 + \mathcal{R})t} \rho_0]_0^\infty \right] \quad (3.44)$$

$$\Phi_T = -k_T \times \operatorname{Tr} \left[\mathbf{P}_T (\mathcal{L}_0 + \mathcal{R})^{-1} \rho_0 \right] \quad (3.45)$$

where $(\mathcal{L}_0 + \mathcal{R})^{-1}$ is the matrix inverse of the sum of the two superoperator matrices.

Chapter 4

Molecular wires

4.1 Experimental results

The remainder of this thesis will concentrate on modelling magnetic field effects on reactivity of the molecules $DMJ-An-FN_1-NDI$ and $DMJ-An-PE_1P-NDI$. From now on these will be referred to as FN_1 and PE_1P respectively. Figure 4.1 displays the molecular structures of these two species. The focus of this thesis

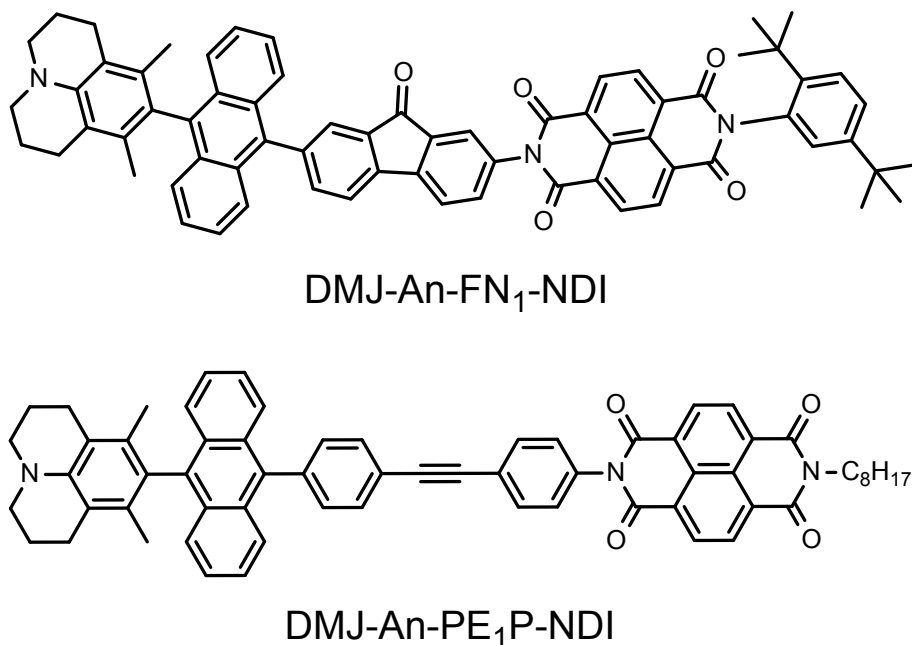


Figure 4.1: Molecular structures.

is to develop a model of the spin dynamics of FN_1 and PE_1P radical pairs which reproduces experimental results by Scott *et al.*^[6].

The experimental photophysics, as observed by Scott *et al.*, are summarised in figure 4.2. The general structure is given by $D-A1-B-A2$ where $D = DMJ$, $A1 = An$, $A2 = NDI$ and $B = FN_1$ or PE_1P . In previous experimental studies, the DMJ-An group is first photoexcited (using 7 ns, 2.5 mJ, 416 nm laser pulses^[6]) into its charge transfer band to form $D^{\cdot+}-A1^{\cdot-}-B-A2$. This excited

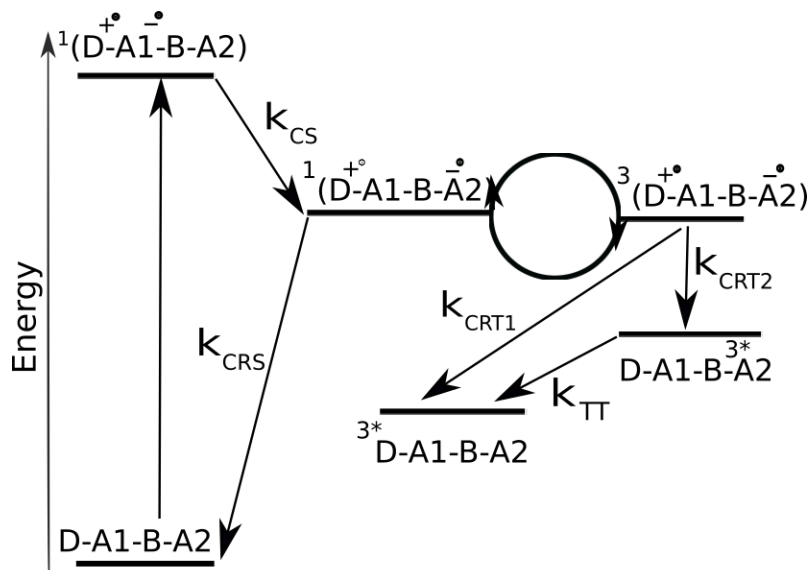


Figure 4.2: Radical Pair Mechanism.

species subsequently undergoes a charge transfer process at a rate k_{CS} to form the singlet radical pair species $D^{\bullet+} - A1 - B - A2^{\bullet-}$. Coherent interconversion then occurs between the excited singlet and excited triplet radical pair states, represented by the curved arrows in figure 4.2. The singlet excited state recombines to give the molecule's ground state at rate k_{CRS} and the triplet excited state can undergo a radical recombination process via two pathways to form distinct excited triplet products. The excited triplet species with the triplet excitation localised on the *DMJ* component is formed at a rate k_{CRT1} and the species with the triplet localised on the *NDI* component is formed at a rate k_{CRT2} . The higher energy product of triplet recombination $D - A1 - B - {}^{3*}A2$ decays to the lower energy state $D^{3*} - A1 - B - A2$ at a rate k_{TT} . The excited triplet state $D - A1 - B - {}^{3*}A2$, which is a product of the triplet recombination pathway, is relatively long lived and therefore was measured using nanosecond transient absorption at 480 nm. The relative triplet yield, calculated by measuring the absorption intensity of long times at each field relative to the absorption at zero field, was reported by Scott *et al.*^[6]. The lifetimes of the radical pair were obtained by fitting individual kinetic traces from nanosecond transient absorption spectra^[6] of the radical pair. Scott *et al.* then used a simple kinetic scheme to extract the spin selective recombination kinetics. The peak relative

triplet yield will occur when the external magnetic field is equal to twice the scalar coupling constant and therefore the value $2J$ can be extracted from MARY curves. The temperature dependence of the scalar coupling constant and the spin selective recombination rates which were calculated using these methods are shown in figure 4.3.

The kinetic model which was used to fit the spin selective recombination rates assumed that there was no coherent evolution of the radical pair states. This assumption motivates the work done in this thesis to calculate the spin selective recombination rates using a model which accounts for the coherent contributions to the spin dynamics, as well as incoherent relaxation effects.

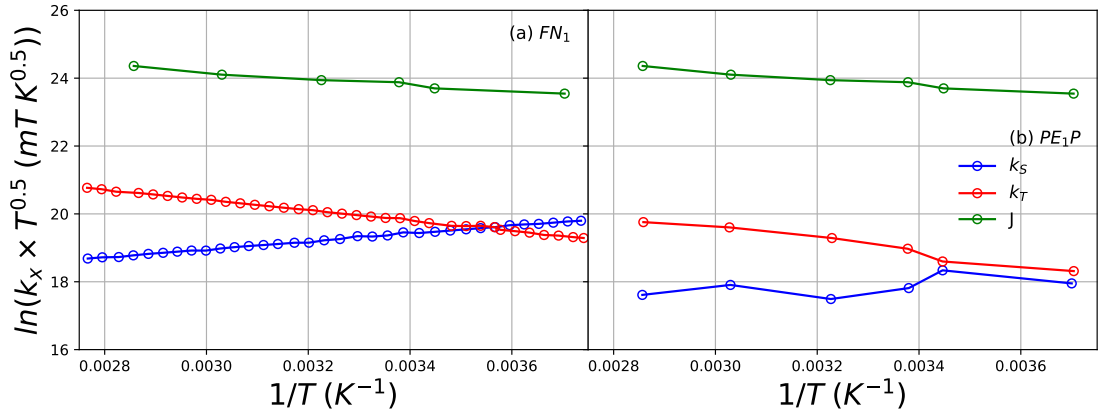


Figure 4.3: Experimental results for rate constants k_S , k_T and reactive scalar coupling J , which Scott *et al.* extracted from their spectroscopic data using a simple incoherent kinetic model^[6].

4.2 Radical pair model

In this section we outline the model for the coherent spin and relaxation processes in these wires. The relaxation mechanisms which determine the evolution of the spin dynamics occur due to rotational diffusion and internal motion of the radical pairs. These effects are included in time dependent fluctuation terms $\hat{V}(t)$ for the system Hamiltonian in equation 2.6. The methods for calculating these fluctuations are outlined in the following section along with how the coherent term \hat{H}_0 is parameterised. All the contributing terms presented in this chapter have a signifi-

cant effect on the radical pair spin dynamics which will be discussed in the following chapter.

4.2.1 Rotational diffusion

Rotational diffusion of the radical pair modulates anisotropic spin-spin coupling interactions and the anisotropic g-tensors of the electron spins. In the Hamiltonian these fluctuations are expressed as^[14]

$$\hat{V}_{rot}(t) = \sum_{n=-2}^{n=2} \sum_{n'=-2}^{n'=2} \mathcal{D}_{n',n}^{(2)}(t) \hat{Q}_{n,n'}^{(2)} \quad (4.1)$$

where $\mathcal{D}_{n',n}^{(2)}(t)$ is the time dependent rank 2 Wigner D-matrix element which is defined by the orientation of the principal axis of the molecule with respect to the lab frame at time t ^[30]. $\hat{Q}_{n,n'}^{(2)}$ is given by

$$\hat{Q}_{n,n'}^{(2)} = \hat{Q}_{1,n,n'}^{(2)} + \hat{Q}_{2,n,n'}^{(2)} + \hat{Q}_{dip,n,n'}^{(2)} \quad (4.2)$$

and

$$\hat{Q}_{i,n,n'}^{(2)} = \mu_B g_{i,n}^{(2)} T_{n'}^{(2)}(\hat{\mathbf{S}}_i, \mathbf{B}_0) + \sum_{k=1}^{N_i} A_{i,k,n}^{(2)} T_{n'}^{(2)}(\hat{\mathbf{S}}_i, \hat{\mathbf{I}}_{i,k}) \quad (4.3)$$

$$\hat{Q}_{dip,n,n'}^{(2)} = D_n^{(2)} T_{n'}^{(2)}(\hat{\mathbf{S}}_1, \hat{\mathbf{S}}_2). \quad (4.4)$$

where $\hat{Q}_{i,n,n'}^{(2)}$ is the anisotropic component of the Hamiltonian for radical i and $\hat{Q}_{dip,n,n'}^{(2)}$ is the dipolar electron spin coupling contribution^[14]. In the above equations, $T_{n'}^{(2)}(\mathbf{u}, \mathbf{v})$ represents the rank 2 spherical tensor components of the vectors \mathbf{u} and \mathbf{v} and $A_{i,k,n}^{(2)}, g_{i,n}^{(2)}, D_n^{(2)}$ are the rank 2 spherical tensor components of the anisotropic hyperfine coupling tensors, the anisotropic g-tensors and the dipolar coupling tensor respectively. The rotational diffusion of the molecule is described by the symmetric top diffusion model. For this model the rank 2 Wigner D-matrix element correlation functions are given by^[14]

$$\langle \mathcal{D}_{m,n}^{(2)}(t)^* \mathcal{D}_{m',n'}^{(2)}(t + \tau) \rangle = \frac{1}{5} \delta_{m,m'} \delta_{n,n'} e^{-(6D_{\perp} + (D_{\parallel} - D_{\perp})n^2)|\tau|} \quad (4.5)$$

where D_{\perp} & D_{\parallel} are the rotational diffusion constants perpendicular and parallel to the molecular symmetry axis.

4.2.2 Internal motion

Internal motion, such as torsional motion of the bridges, of the radical pair modulates the scalar electron spin coupling interaction. The correlation time of these fluctuations is assumed to be orders of magnitude smaller than the timescales of spin dynamics^[31]. Consequently the extreme narrowing limit can be applied and the contribution of the internal motion to the dephasing of the singlet and triplet states is given by the phenomenological term,

$$\mathcal{R}\hat{\rho}(t) = -k_D \left(P_S \hat{\rho}(t) P_T + P_T \hat{\rho}(t) P_S \right). \quad (4.6)$$

The dephasing rate constant k_D is difficult to ascertain a priori and therefore it will be parameterised via maximum likelihood estimation, as described later.

An approximate expression for k_D evaluated using the correlation function in the extreme narrowing limit is given by $k_D = 4(\tau_c) \langle \Delta J^2 \rangle$. In general, assuming harmonic motion and a linear dependence of J on the normal mode displacements, the average $\langle \Delta J^2 \rangle$ is proportional to the temperature and the timescale τ_c is proportional to friction in the system. However in the model used it will be assumed that the dephasing rate is constant and not dependent upon temperature.

4.3 Electronic transitions

The spin selective rate constants and the scalar coupling constant are challenging to calculate from first principles and therefore, in order to determine the temperature dependence of these variables, parameters for approximate rate laws will be found using maximum likelihood estimation.

4.3.1 Extended Marcus-Hush theory

Marcus-Hush theory predicts that the rate of electron transfer is given by

$$k_X = \left(\frac{\Delta_X^2}{\hbar} \right) \left(\sqrt{\frac{\pi}{k_b T \lambda_X}} \right) e^{-(\lambda_X + \Delta G_X)^2 / (4 \lambda_X k_b T)} \quad (4.7)$$

where $X = S$ or T for the singlet and triplet recombination rates respectively. Here ΔG_X is the free energy difference between the singlet or triplet radical pair and product states and $\Delta_X = \Delta_S$ or Δ_T is the diabatic coupling between these states^{[32][33]}. λ_x is the reorganisation energy for the transition from the singlet and triplet states. Recently a formalism for the reactive scalar electron spin coupling has been developed which, in the non-adiabatic limit, is dependent only upon the parameters which appear in the Marcus-Hush rate expression^[24]. This contribution is found to be non negligible in many regimes and is given by the equation

$$J_X = \left(\frac{\Delta_X^2}{4}\right) \left(\sqrt{\frac{\pi}{k_b T \lambda_X}}\right) F((\epsilon_X - \lambda_X)/(2\sqrt{k_b T \lambda_X})). \quad (4.8)$$

Here the Dawson F-function is defined in terms of the imaginary error function as,

$$F((\epsilon_X - \lambda_X)/(2\sqrt{k_b T \lambda_X})) = e^{-(\lambda_X - \epsilon_X)^2/(4\lambda_X k_b T)} \operatorname{erfi}\left(\frac{\epsilon_X - \lambda_X}{2\sqrt{k_b T \lambda_X}}\right). \quad (4.9)$$

4.3.2 Exponential Model

A model for the temperature dependence of the spin selective rate constants, k_X , and exchange coupling is the following set of equations which arise from complex electron transfer mechanisms^[34]. This model can explicitly include contributions from negatively activated transitions as the terms E_X are allowed to take negative values during the maximum likelihood estimation procedure and therefore, in light of the experimental results, this model for the rate law will be used. The expressions used in this model are as follows,

$$k_X(T) = \left(\frac{\alpha_X}{\sqrt{T}}\right) e^{-E_X/RT} \quad (4.10)$$

$$J(T) = \left(\frac{J_a}{\sqrt{T}}\right) e^{-J_b/RT}, \quad (4.11)$$

where $X = S$ or T for the singlet and triplet recombination rates respectively. Here α_S , α_T , E_S , E_T , J_a , and J_b are the free parameters for the model which will be estimated using the maximum likelihood method.

4.4 Triplet yield correction at high fields

Observations of field dependent radical pair recombination reactions have found that there is often a field-independent background contribution to the relative triplet yield^[6]. When there is no external magnetic field the triplet states are degenerate and therefore have equivalent transition probabilities from the singlet state via hyperfine-mediated intersystem crossing. However, when the external magnetic field becomes sufficiently large, the $|T_+\rangle$ and $|T_-\rangle$ states will be energetically inaccessible to this reaction pathway. It would therefore be expected that the triplet yield would be one third of that at zero field. This is found not to be the case and instead the relative triplet yield at high fields is significantly larger than $\frac{1}{3}$ ^[35].

Models with a background contribution to the triplet yield have been quantitatively shown to be in better agreement with experimental results^{[35] [36] [37]}. In this thesis three distinctive pathways have been investigated which may give rise to the additional contribution to the triplet yield at high fields. The initial triplet population is the primary mechanism that will be considered and the other two contributions will be compared at the end of the results chapter.

4.4.1 Initial triplet population

It is possible that in the initial charge separation step a fraction of triplet states are generated which then recombine via the triplet recombination pathway^{[38] [37] [36]}.

Thus the initial density matrix operator can be written as

$$\langle \hat{\rho}(0) \rangle = \frac{1 - \lambda_T}{Z} \hat{P}_S + \frac{\lambda_T}{3Z} \hat{P}_T \quad (4.12)$$

where λ_T is the initial triplet fraction which will be obtained via maximum likelihood estimation.

4.4.2 Intersystem crossing

The singlet recombination reaction may be accompanied by an incoherent intersystem crossing, mediated by spin-orbit coupling, to yield a triplet product from the singlet radical pair state^[14]. If the rate of this intersystem crossing reaction is defined as k_{ST} then the observed triplet quantum yield is described by the relation

$$\phi_{T,obs} = \phi_T + \frac{k_{ST}}{k_S} \phi_S = \left(\frac{k_S - k_{ST}}{k_S} \right) \phi_T + \frac{k_{ST}}{k_S} \quad (4.13)$$

where $\phi(B)$ is the triplet yield calculated without intersystem crossing and k_S is the total singlet recombination rate. The relative triplet yield is therefore given by

$$RTY(B) = \frac{\phi(B) + \frac{k_{ST}}{k_S - k_{ST}}}{\phi(0) + \frac{k_{ST}}{k_S - k_{ST}}} = \frac{\phi(B) + x_0}{\phi(0) + x_0} \quad (4.14)$$

where $x_0 = k_{ST}/(k_S - k_{ST})$ is a background contribution to the relative triplet yield which can be used to calculate the rate of intersystem crossing. We will approximate x_0 as temperature independent which is valid if k_{ST} and k_S have a similar temperature dependence.

4.4.3 Additional spin relaxation

Additional contributions to the spin relaxation can result in a field independent contribution to the triplet yield. It is challenging to model a priori all relaxation mechanisms and therefore the additional contributions are included by phenomenologically introducing a term into the Liouvillian^{[7] [36]}. These transitions are modelled by the addition of an incoherent kinetic term to the Liouville superoperator which is given by

$$\begin{aligned} \mathcal{L}_{relax} \hat{\rho}(t) = & k_{relax} \sum_m \left(-\frac{1}{2} \left\{ |S\rangle \langle S| + |T_m\rangle \langle T_m|, \hat{\rho}(t) \right\} \right. \\ & \left. + |S\rangle \langle T_m| \hat{\rho}(t) |T_m\rangle \langle S| + |T_m\rangle \langle S| \hat{\rho}(t) |S\rangle \langle T_m| \right). \end{aligned} \quad (4.15)$$

4.5 Parameterisation

The minimum energy structures and physical parameters which define the principle interaction terms need to be calculated and transformed into the correct frame

of reference before the models described above can be used to reproduce the experimental results.

4.5.1 Anisotropic hyperfine and g-tensor interaction terms

The minimum energy structural conformations for the radicals capped by hydrogens, were calculated with DFT using the B3LYP functional and 6-31G(d,p) basis set with the D3 dispersion correction, as implemented in Gaussian09^[14]. Isotropic components of the hyperfine coupling tensors, $a_{iso} = (A_{xx} + A_{yy} + A_{zz})/3$, for the $NDI^{\cdot-}$ radical are taken from experimental results in reference^[39]. The signs of the isotropic components and the anisotropic components are obtained from DFT as described. The hyperfine coupling tensors were then calculated with the B3LYP functional and the EPR-III basis set for this optimised geometry for each radical in isolation^[14]. The anisotropic g-tensors were calculated analogously^[14]. All DFT calculations were performed by Thomas Fay.

4.5.2 Dipolar coupling tensors

Dipolar coupling tensors are calculated using the point dipole approximation, assuming two radicals lie on the molecular z-axis and taking the gyromagnetic ratio to be equal to that of a free electron. In the principal axis frame (P.A.F.) the dipolar coupling tensor is given by

$$\hat{\mathbf{D}}_{(P.A.F.)} = \left(-\frac{\mu_0 \gamma_e^2 \hbar^2}{4\pi r_{S_1, S_2}^3}\right) \begin{bmatrix} 1 & 0 & 0 \\ 0 & 1 & 0 \\ 0 & 0 & -2 \end{bmatrix}. \quad (4.16)$$

4.5.3 Frames of reference

The hyperfine tensors were calculated in the radical principal axis frame, however they are required for the simulations to be in the molecular principal axis frame and as such a transformation is required. To transform the current reference frame to a new reference frame, the axes of the new frame are specified by vectors $\mathbf{n}_1, \mathbf{n}_2, \mathbf{n}_3$

in the old frame. For a vector \mathbf{V} in the old frame a vector \mathbf{V}' in the new frame is define by

$$\mathbf{V}' = \mathbf{N}^T \cdot \mathbf{V} \quad (4.17)$$

where $\mathbf{N} = (\mathbf{n}_1, \mathbf{n}_2, \mathbf{n}_3)$. Hence the coupling tensors for operators in the new frame are given by

$$\mathbf{A}' = \mathbf{N}^T \cdot \mathbf{A} \cdot \mathbf{N}. \quad (4.18)$$

Given the dipolar coupling tensor is known in the molecular principal axis frame, it is convenient to convert all interaction tensors into this frame of reference. The transformation of the radical principal axis frames to the molecular principal axis frame is found using the eigenvectors of the respective inertia tensors to define the transformation tensor \mathbf{N} . The inertia tensor \mathbf{I} for a system is given by

$$\mathbf{I} = \begin{bmatrix} \sum_{\alpha} m_{\alpha}(y_{\alpha}^2 + z_{\alpha}^2) & -\sum_{\alpha} m_{\alpha}(x_{\alpha}y_{\alpha}) & -\sum_{\alpha} m_{\alpha}(x_{\alpha}z_{\alpha}) \\ -\sum_{\alpha} m_{\alpha}(y_{\alpha}x_{\alpha}) & \sum_{\alpha} m_{\alpha}(z_{\alpha}^2 + x_{\alpha}^2) & -\sum_{\alpha} m_{\alpha}(y_{\alpha}z_{\alpha}) \\ -\sum_{\alpha} m_{\alpha}(z_{\alpha}x_{\alpha}) & -\sum_{\alpha} m_{\alpha}(z_{\alpha}y_{\alpha}) & \sum_{\alpha} m_{\alpha}(x_{\alpha}^2 + y_{\alpha}^2) \end{bmatrix}. \quad (4.19)$$

4.5.4 Stokes-Einstein equation

The rigid prolate symmetric top rotational diffusion coefficients were approximated by searching through all atoms to find those with the greatest displacements from each axis, within the principal axis frame of reference, and calculated according to

$$r_{\perp} = r_z \quad \& \quad \frac{1}{r_{\parallel}^3} = \frac{1}{2} \left(\frac{1}{r_x^3} + \frac{1}{r_y^3} \right) \quad (4.20)$$

where r_z is the length from the origin along the z-axis to the atom with the greatest displacement along this axis.

The rotational diffusion coefficients were calculated using the Stokes-Einstein equation^[40],

$$D_{\alpha} = \frac{k_B T}{8\pi\eta r_{\alpha}^3}, \quad (4.21)$$

where $\alpha = \parallel$ or \perp and r_{\parallel} and r_{\perp} for diffusion are the effective radii parallel and perpendicular the molecular symmetry axis respectively. The parameter η is the

dynamic viscosity of the solution.

4.5.5 Viscosity of toluene

The parameter η has a temperature dependence which needs to be included in the model. The experiments were conducted with the molecules of interest in a solution of toluene. The dynamic viscosity is fitted using an Arrhenius type temperature dependence, $\eta = Ae^{B/T} + C$, where A is a pre-exponential factor, B is related to the activation energy for viscous flow in the liquid and C a temperature independent contribution.^[41]

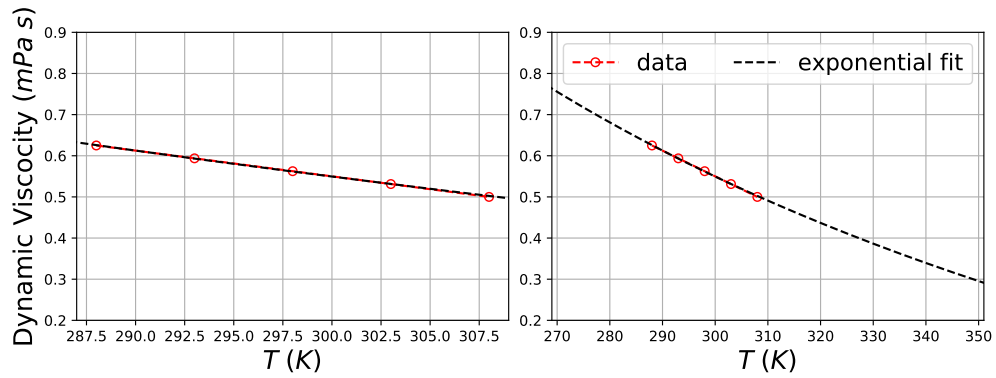


Figure 4.4: Temperature dependence of the viscosity of toluene.

Figure 4.4 shows the fitted functional equation $\eta = Ae^{B/T} + C$ where it is found that $A = 3.92904692 \times 10^3 (\text{Pa} \cdot \text{s})$, $B = 9.96973104 \times 10^{+1} (\text{K})$ & $C = -4.92846450 \times 10^{-3} (\text{Pa} \cdot \text{s})$.

4.6 Maximum likelihood parameter estimation

The code written for the investigation of the dynamics of these radical pair systems outputs the relative triplet yield and the radical pair lifetime for a particular value of the external magnetic field, dependent upon parameters including the J-coupling and the singlet and triplet recombination rates. These parameters can be formulated in terms of their temperature dependence from approximate equations given previously. Consequently, using the theory of maximum likelihood estima-

tion, the kinetic equations which describe the exchange coupling and the singlet and triplet recombination rates can be parameterised. Parameters including contributions to the observed field-independent background contribution to the relative triplet yield as well as a singlet-triplet dephasing term will also be estimated using this method.

In a parameter estimation problem, information about a parameter is obtained from a sample of data by analysis of the underlying probability distribution. There is some underlying true set of parameters a_{true} that are realised physically but are hidden to the experimenter. These true parameters are statistically realised, combined with random measurement errors, as a measured data set which is denoted D_0 . The experimenter fits the data to a model, obtaining a parameter set a_0 . As the measurement errors have a random component, D_0 is not a unique realisation of the true parameters a_{true} . Instead there are infinitely many ‘hypothetical’ measurement data sets, denoted D_0, D_1, D_2, \dots . Each of these data sets, had they been realised, would have lead to different parameter sets a_0, a_1, a_2, \dots . These parameter sets a_i occur with a probability distribution in the M dimensional space of all possible parameter sets and the actual measured set a_0 is drawn from this distribution. The distribution of the difference $a_i - a_{true}$ has the true value at the origin and as such knowledge of this distribution would allow us to infer the quantitative uncertainties in our experimental measurement a_0 ^[42].

For a Gaussian distribution of measurement noise with varying standard deviation, σ_i , the probability of the data set being generated by the parameters is:

$$P \propto \prod_{i=1}^N e^{-(y_i - f(x_i))^2 / (2\sigma_i^2)} \quad (4.22)$$

where y_i is the experimental data point, $f(x_i)$ is the model data point. Maximising this probability involves minimising the χ^2 function of weighted residuals:

$$-\ln(P) = \chi^2 = \sum_{i=1}^N \frac{(y_i - f(x_i))^2}{2\sigma_i^2} \quad (4.23)$$

where the unbiased σ is estimated by $\sigma^2 = \frac{1}{n-1} \sum_{i=1}^n (f(x_i) - \bar{f})^2$ and $\bar{f} = \frac{1}{n} \sum_{i=1}^n f(x_i)$.

The sum of the χ^2 functions, calculated in this way for the lifetimes and relative

triplet yields at each temperature, is minimised to find the parameters for the model. The objective function is non-linear and multi-dimensional and therefore the minimum cannot be found analytically. Hence the differential evolution method was used, which provides a robust estimate of the global minimum. Differential evolution is a stochastic, direct search, evolutionary optimisation algorithm proposed by Storn and Price^[43]. At each iteration, called a generation, new candidate solutions, called agents, are generated stochastically by the combination of agents chosen from the current population. This new agent is combined with a predetermined target agent to form the trial vector of the iteration in a process termed recombination. The trial vector will be selected to become an agent in the next generation if it reduces the current minimum value of the objective function. This algorithm is relatively simple and robust in that it is less likely to converge on local minima than standard minimisation routines such as the method of Nelder and Mead^[44].

Chapter 5

Results and discussion

This chapter firstly presents the results of fitting the model described in Chapter 4, to the experimental results obtained by Scott *et al.*^[6] for the FN_1 and PE_1P radical pairs. The simulated lifetimes and MARY curves for the model are displayed with the experimental curves, along with the best fit parameters. The initial triplet population was found to be the most successful way to simulate the background triplet yield and therefore the results in this chapter will use this mechanism unless stated otherwise. The second half of this chapter discusses the physical significance of the fitted parameters and what can subsequently be learned about electron transfer in these systems.

5.1 Results

In this section, the simulations of the lifetimes and MARY curves for the PE_1P and FN_1 radical pairs will be quantitatively compared to the experimental results. Firstly we compare the percentage difference in lifetime at each temperature for zero field, experimental resonant field ($B = 2J_{exp}$), and high field. Secondly the Nash–Sutcliffe model efficiency coefficient (NSE)^[45], which is equivalent to the general form of the commonly used R^2 coefficient, of the MARY curve is calculated for each molecule at each temperature. The value of NSE is given by

$$NSE = 1 - \frac{\sum_i^N (RTY_{exp}(B_i) - RTY_{sim}(B_i))^2}{\sum_i^N (RTY_{exp}(B_i) - \overline{RTY}_{exp})^2} \quad (5.1)$$

where $RTY_{exp}(B_i)$ and $RTY_{sim}(B_i)$ are the sets of experimental and simulated relative triplet yield values respectively and \overline{RTY}_{exp} is the mean experimental relative triplet yield. The ideal value of NSE, corresponding to a perfect fit to the experimental data, is 1. The mean NSE value for a superposition of Lorentzian functions fitted individually to each MARY curve is $NSE = 0.942$ for PE_1P and $NSE = 0.967$ for FN_1 which indicates what a good value of NSE should be given the errors in the

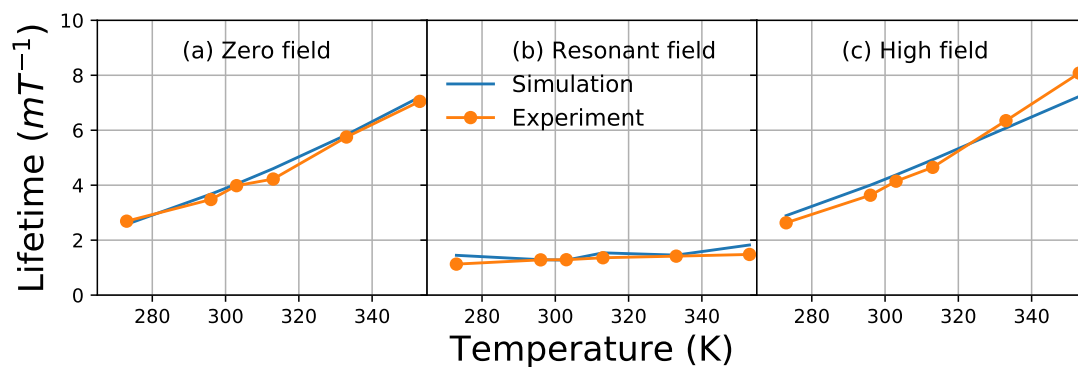
experimental data. The NSE coefficient gives an indication of the goodness of fit of a model compared to a straight line at the mean value of all the experimental data points. The NSE coefficient is, however, sensitive to extreme values and if there is a significant deviation from the experimental data then the sum of the squares of differences is larger for the model than for the straight line at the mean value and therefore the NSE coefficient will become negative.

For the exponential rate law model with dephasing and an initial triplet population for the background yield the percentage difference in lifetime and the *NSE* values are presented in Table 5.1 and 5.2 for the the FN_1 and PE_1P radical pairs respectively. All simulations during the minimisation procedure were converged using 400 Monte-Carlo samples at each magnetic field value. The corresponding MARY curves and lifetimes are plotted in figures 5.1 and 5.2. In the figures it is observed that the model simulates the experimental MARY traces more accurately at low and high fields and deviates the most around the resonant, $B \approx 2J$, field strength.

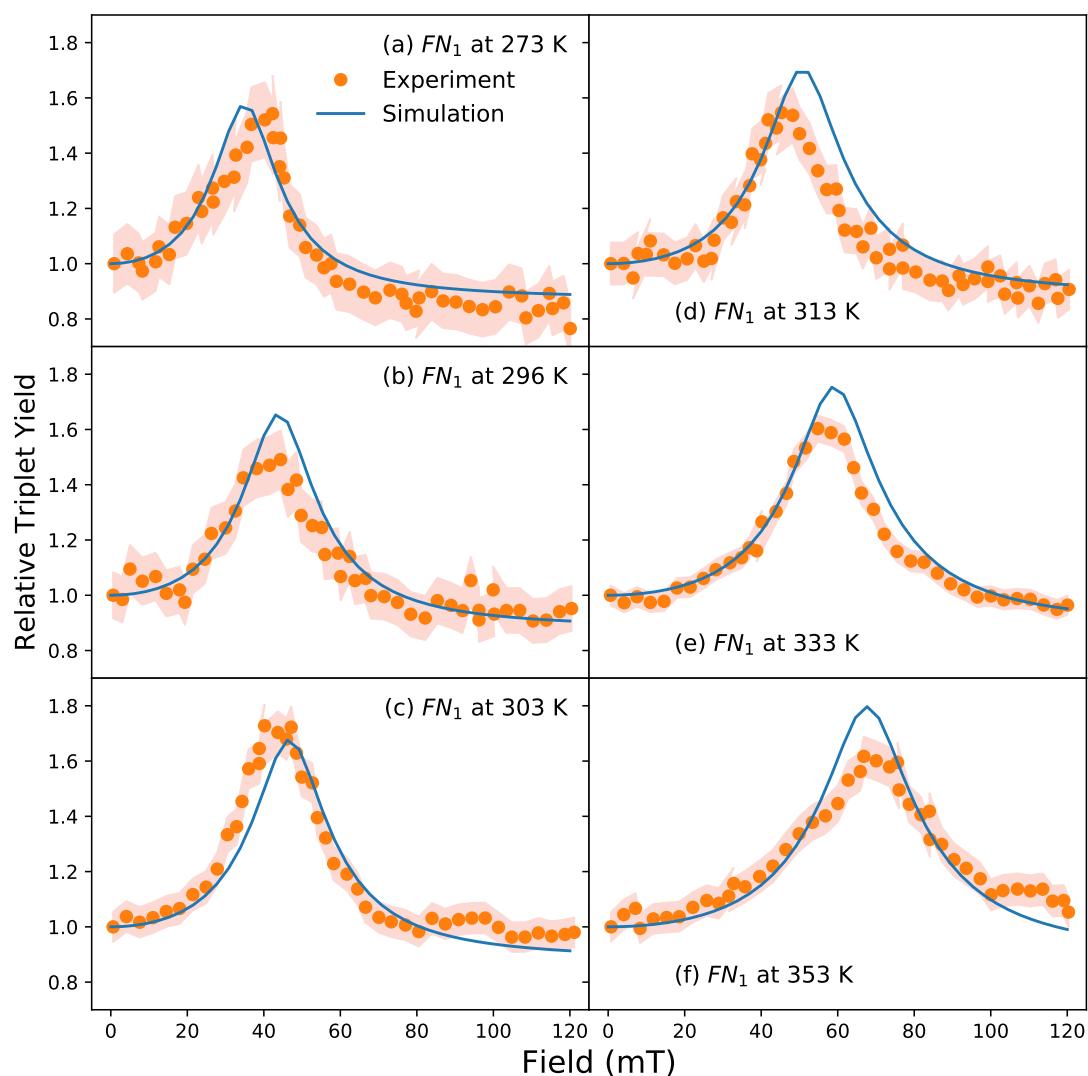
The percentage differences in the radical pair lifetimes are larger for the PE_1P radical pair although this appears to be because there is more noise in the experimental data. This is also the case for the discrepancy at high field for PE_1P at 270 *K* and at the resonant field strength at 310 *K*. The error bars in figure 5.1 and 5.2 are estimated experimental errors however there may be other systematic errors present in the experimental data.

Temperature	<i>NSE</i>	diff zero B (%)	diff res B (%)	diff high B (%)
273	0.876	-6.681	+24.627	+6.584
296	0.835	+2.075	-2.695	+6.389
303	0.876	-1.906	-4.188	+1.944
313	0.756	+5.254	+9.522	+2.352
333	0.911	-2.077	-0.496	-7.493
353	0.864	-1.259	+19.314	-13.567
Mean	0.853	3.209	10.140	6.388

Table 5.1: Quantitative comparison of results for FN_1 using the exponential model.

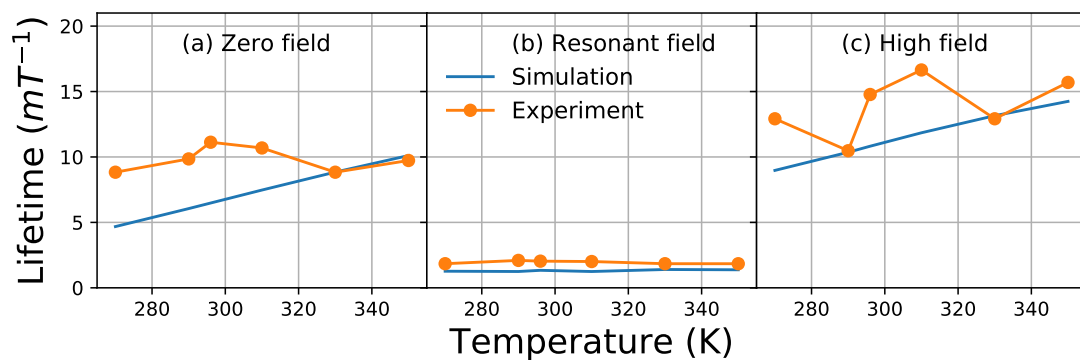


(a) Radical pair lifetimes

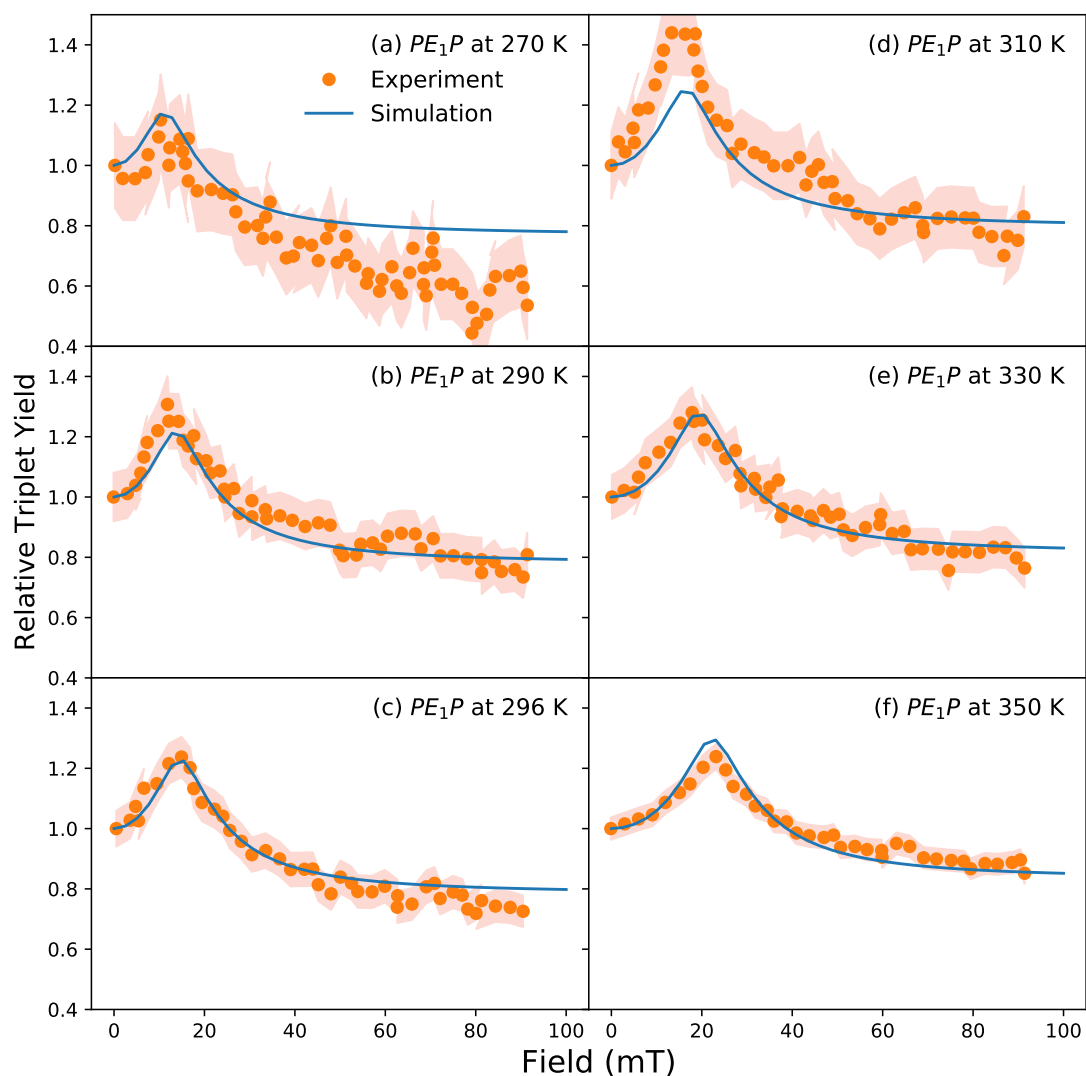


(b) MARY curves, the shaded area represents an estimate for two standard errors at each experimental data point.

Figure 5.1: Comparison of the simulation and experimental results for FN_1 molecule.



(a) Radical pair lifetimes



(b) MARY curves, the shaded area represents an estimate for two standard errors at each experimental data point.

Figure 5.2: Comparison of the simulation and experimental results for PE_1P molecule.

Temperature	NSE	diff zero B (%)	diff res B (%)	diff high B (%)
270	0.332	-48.300	-30.501	-31.269
290	0.905	-38.534	-40.474	-1.114
296	0.932	-41.749	-34.366	-26.750
310	0.775	-30.087	-37.956	-28.833
330	0.922	+0.094	-24.016	+1.825
350	0.885	+3.867	-25.150	-9.229
Mean	0.792	27.105	32.077	16.503

Table 5.2: Quantitative comparison of results for PE_1P using the exponential model.

Molecule	$a_T(K^{1/2}s^{-1})$	$Ea_T(kJ\ mol^{-1})$	$a_S(K^{1/2}s^{-1})$	$Ea_S(kJ\ mol^{-1})$
FN_1	5.412×10^{10}	+2.017	6.193×10^6	-8.597
PE_1P	2.383×10^9	-1.901	1.242×10^7	-3.512

Molecule	$J_a(K^{1/2}s^{-1})$	$J_b(kJ\ mol^{-1})$	λ	$k_D(s^{-1})$
FN_1	5.645×10^{10}	+6.600	0.429	1.45×10^7
PE_1P	2.018×10^{10}	+6.773	0.456	8.96×10^6

Table 5.3: Fitted parameters for exponential rate law.

The parameters fitted using maximum likelihood estimation for the exponential rate model are displayed in Table 5.3. For both the FN_1 and the PE_1P molecules the reactive scalar coupling interaction is positively activated by a value of the same order of magnitude. The triplet recombination transition is positively activated for the FN_1 molecule while the singlet recombination process is negatively activated. For the PE_1P molecule, however, the singlet and triplet recombination transitions are both negatively activated.

Figure 5.3 shows the temperature dependence of the simulated scalar coupling and spin selective recombination rates and compares them to the results obtained using a simple kinetic model. It is interesting that, when comparing these rate models to the simple kinetic scheme used to analyse the results in the experimental paper^[6], the rate of triplet recombination is orders of magnitude larger. This discrepancy highlights the importance of simulating systems of this type by modelling the coherent evolution of the spin states rather than using a simple incoherent kinetic scheme.

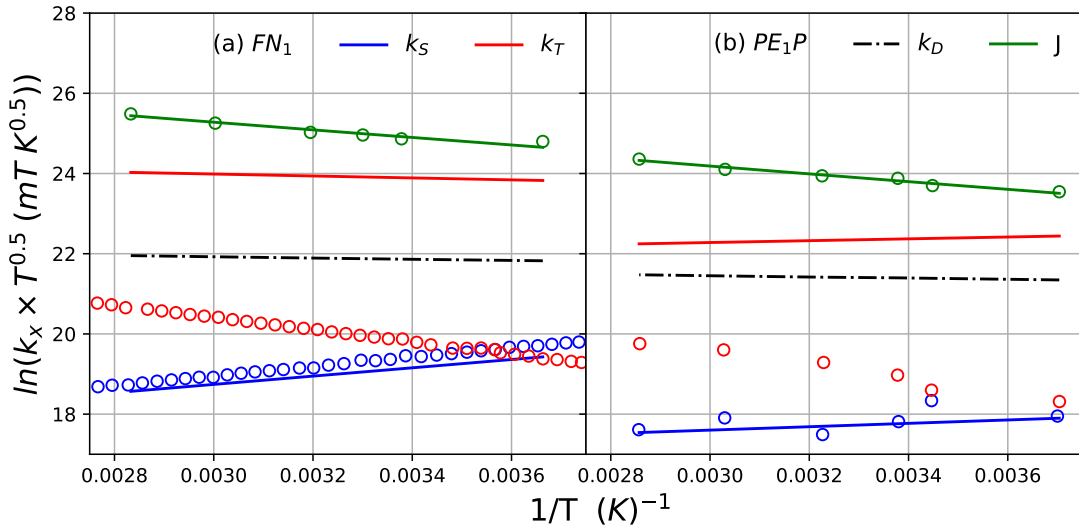


Figure 5.3: Temperature dependence of rate constants where the circles are the data points extracted by the Scott *et al.* and the solid lines are calculated using the fitted exponential model.

5.2 Discussion

The most interesting result of the previous section is the observation of electronic transitions with negative effective activation energies. This section will focus on the discussion of the physical implications of this result. Following which the observations about the dephasing and background yield contributions will also be explored.

5.2.1 Mechanisms of electron transfer

It is important to understand the mechanism of an electronic transition when discussing its observed temperature dependence. The electron transfer between two ends of a molecular wire can proceed by one of two competing mechanisms, both of which are outlined in figure 5.4.

Coherent tunnelling, otherwise known as the superexchange model of electron transfer, requires that the donor and acceptor motifs are energetically separated from the bridge states. The bridge couples the orbitals of the donor and acceptor sites and mediates the electronic transition^[46]. Crucially the bridge itself is not formally

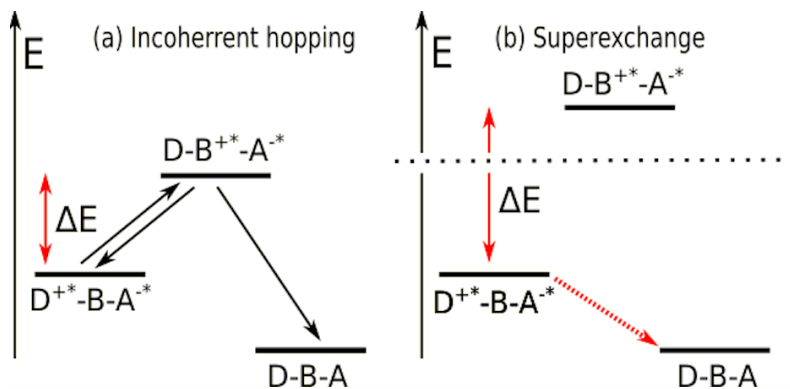


Figure 5.4: Electronic transition mechanisms. In (a) $\Delta E \approx K_B T$ and in (b) $\Delta E \gg K_B T$

oxidised or reduced during the process of electron transfer. The rate of the single tunnelling step in the superexchange reaction is controlled by the overlap of bridges and donor/acceptor orbitals and hence decreases exponentially as the separation between the donor and acceptor groups increases^[47]. This electron transfer pathway should therefore be successfully approximated by the Marcus theory equation, where Δ_X^2 is the effective superexchange coupling^[48].

The incoherent hopping mechanism is often referred to as thermally activated hopping as it involves real intermediate states that actively transport the electron along the wire^[49]. The electron or hole initially hops onto the bridging component of the molecule and then rapidly recombines as the electronic coupling is now much stronger due to the reduced spatial separation. It is found that, due to greater stabilisation of charge, the rate of hopping mediated recombination increases as the length of the bridging motif increases^[50]. For the molecules discussed in this thesis, PE_1P and FN_1 , the charge recombination pathway for both the singlet and triplet reactions has been suggested to be dominated by the superexchange mechanism^[51]. This suggestion will be scrutinised below.

5.2.2 Negative activation Energy

The negatively activated singlet recombination in the FN_1 molecule, predicted by Scott *et al.*^[6] using a simple kinetic analysis, has been shown to be accurate by conducting the analysis with a more physically realistic calculation which involved the

coherent evolution of the spin dynamics as well as incoherent relaxation. Many explanations have been proposed for this observation, some of which are outlined in this discussion, followed by a new proposal and an analysis using the Nakajima-Zwanzig equation. It is also worth reiterating that the singlet recombination pathway is thought to be dominated by a superexchange mechanism,^[12] despite being deep in the Marcus inverted region, due to the large electronic coupling term^[35]. The model we have used has also shown the singlet and triplet recombination transitions in the PE_1P molecule to be negatively activated and the following discussion applies to these processes as well.

Perhaps the most intuitive explanation for the negative activation energies is that thermally activated torsional motions may disrupt the conjugation between donor and acceptor orbitals and thus lower the effective coupling^[52]. However, this is unlikely given that in the ground state conformation the donor and acceptor conjugated π -systems are approximately perpendicular to bridging orbitals such that torsional motions would increase the orbital overlap.

Alternatively, the electron tunnelling process may be mediated by a solvent mechanism. At lower temperatures the dynamic solvent effects dominate and the charge transfer becomes adiabatic. This mechanism requires that the longitudinal relaxation time of the solvent to be of the same order of magnitude as the time constant of the charge transfer^[53]. However in the reactions studied in this thesis the solvent is toluene which is non-polar and will therefore be only very weakly coupled to the electron transfer. Consequently the solvent mechanism will not become dominant at the temperatures at which the experiments were conducted.

In systems where the final electronic surface crosses the initial state near its minimum, equivalent to a process with no activation barrier, the lower lying vibrational states are the most reactive^[12]. Thermal population of higher lying vibrational reactant states decreases the population of vibrational states coupled to the reaction coordinates which slows the electron transfer process. This requires that the mag-

nitude of the driving force for recombination equals the reorganisation energy for the recombination which is not the case for the singlet recombination in FN_1 as the reaction lies deep in the Marcus inverted regime^[54]. For both radical pairs the triplet recombination is estimated, by Scott *et al.*^[6], to occur near the maximum of the Marcus rate curve ($|\Delta G_T| \approx \lambda_T \approx 0.5$ eV) whereas the singlet recombination lies deep in the Marcus inverted region ($|\Delta G_S| \approx 2.3$ eV and $\lambda_S \approx 0.5$ eV) therefore this cannot explain the observed negative activation energy of singlet recombination.

A kinetic conformational pre-equilibrium model has also been suggested to account for the phenomena of a negatively activated recombination pathway in which the intermediate is a reactive conformation of the molecule^[55]. Here we shall apply a similar analysis using the Nakajima-Zwanzig formalism to the density matrix of a system in which the intermediate is another radical pair state, as in the hopping mechanism. This treatment of a hopping mediated reaction model is more plausible in the present context and as such we shall not discuss the conformational pre-equilibrium model any further.

5.2.3 An intermediate radical pair state

The negative activation energy can potentially be explained by the existence of two radical pair forms which are distinguished by the part of the molecule on which the radical species are localised. The radical pair is initially formed, after charge separation, in the singlet state with the unpaired electrons localised on the donor *DMJ* and acceptor *NDI* motifs (RP_1). One of the unpaired electrons or holes can migrate onto the bridging component of the molecule (at a rate k_f) to form RP_2 . There is also a competing backwards reaction in which RP_1 is reformed at a rate k_b . Both radical pair species can undergo charge recombination reactions from their singlet and triplet states with rates $k_{S,1}$, $k_{S,2}$ and $k_{T,1}$, $k_{T,2}$ respectively to form product states (P_T and P_S) as shown in figure 5.5. For the two molecules studied in this thesis, PE_1P and FN_1 , we will propose that the intermediate radical pair

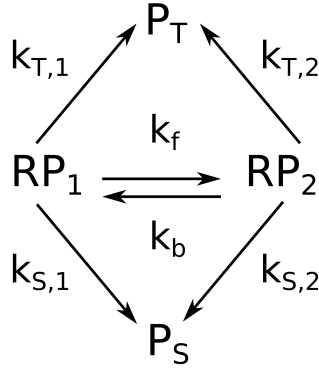


Figure 5.5: Reaction scheme

state RP_2 is $DMJ - An^{\cdot+} - B - NDI^{\cdot-}$. Despite the HOMO for this species being higher in energy than that of RP_1 , $DMJ^{\cdot+} - An - B - NDI^{\cdot-}$, the electron hole is closer to the negative charge and therefore the species is electrostatically stabilised.

The evolution of this model of the system can be described by the set of differential equations

$$\frac{d}{dt}\rho_1(t) = \mathcal{L}_1\hat{\rho}_1(t) - k_f\hat{\rho}_1(t) + k_b\hat{\rho}_2(t) \quad (5.2)$$

$$\frac{d}{dt}\rho_2(t) = \mathcal{L}_2\hat{\rho}_2(t) + k_b\hat{\rho}_1(t) - k_f\hat{\rho}_2(t) \quad (5.3)$$

where \mathcal{L}_i is the Liouville superoperator for radical pair i and the indices 1 and 2 correspond to the two species RP_1 and RP_2 . This is equivalent to

$$\frac{d}{dt}\hat{\rho}(t) = \mathcal{L}\hat{\rho}(t) \quad (5.4)$$

where $\hat{\rho}(t) = \left(\hat{\rho}_1(t), \hat{\rho}_2(t)\right)^T$ and

$$\mathcal{L} = \begin{pmatrix} \mathcal{L}_1 - k_f & k_b \\ k_f & \mathcal{L}_2 - k_b \end{pmatrix}. \quad (5.5)$$

The radical is initially in state 1 and therefore a projection operator \mathcal{P} is defined such that

$$\mathcal{P} = \begin{pmatrix} 1 & 0 \\ 0 & 0 \end{pmatrix} \quad \text{and} \quad \mathcal{P}\hat{\rho}(0) = \hat{\rho}(0). \quad (5.6)$$

Its complement is analogously defined as

$$\mathcal{Q} = \begin{pmatrix} 0 & 0 \\ 0 & 1 \end{pmatrix} \quad (5.7)$$

where $\mathbf{1} = \mathcal{P} + \mathcal{Q}$. The equation of motion for the projected density matrix can be shown to be

$$\frac{d}{dt}\mathcal{P}\hat{\rho}(t) = \mathcal{P}\mathcal{L}\mathcal{P}\hat{\rho}(t) + \int_0^t d\tau \mathcal{P}\mathcal{L}\mathcal{Q}e^{\mathcal{Q}\mathcal{L}(t-\tau)}\mathcal{Q}\mathcal{L}\mathcal{P}\hat{\rho}(\tau). \quad (5.8)$$

The time integrated density operator from which physical observables of the system dynamics can be calculated is then given by

$$\int_0^\infty dt \mathcal{P}\hat{\rho}(t) = -(\mathcal{P}\mathcal{L}\mathcal{P} + \mathcal{K})^{-1}\mathcal{P}\hat{\rho}(0) \quad (5.9)$$

where the kernel is given by

$$\mathcal{K} = \int_0^\infty dt \mathcal{P}\mathcal{L}\mathcal{Q}e^{\mathcal{Q}\mathcal{L}t}\mathcal{Q}\mathcal{L}\mathcal{P} \quad (5.10)$$

$$\mathcal{K} = \int_0^\infty dt \mathcal{P}\mathcal{L}\mathcal{Q}e^{\mathcal{Q}\mathcal{L}\mathcal{Q}t}\mathcal{Q}\mathcal{L}\mathcal{P} \quad (5.11)$$

$$\mathcal{K} = -\mathcal{P}\mathcal{L}\mathcal{Q}(\mathcal{Q}\mathcal{L}\mathcal{Q})^{-1}\mathcal{Q}\mathcal{L}\mathcal{P}. \quad (5.12)$$

In order to evaluate \mathcal{K} we assume that all hyperfine and Zeeman interaction terms for \mathcal{L}_2 can be neglected within the kernel. This approximation is valid because the scalar coupling and the decay rates of RP_2 are likely to be significantly larger than the other terms in the Liouvillian. This approximation ensures that $\mathcal{Q}\mathcal{L}\mathcal{Q}$ is diagonal in the singlet-triplet basis set ($\langle n| = \langle S|, \langle T_{+1}|, \langle T_0|, \langle T_{-1}|$), giving

$$\mathcal{K} = -\sum_{n,m} |n, m\rangle \langle n, m| \frac{k_f k_b}{-(1/2)(k_{n,2} + k_{m,2}) - k_b - i(\epsilon_{n,2} - \epsilon_{m,2})} \quad (5.13)$$

where $|n, m\rangle \equiv |n\rangle \langle m|$ and $\epsilon_{n,2}$ is the energy of state n under the reduced Liouvillian such that $\epsilon_{S,2} = +J_2$ and $\epsilon_{T_{m,2}} = -J_2$. Therefore the effective rate constants $k_{n,eff}$ are given by

$$k_{n,eff} = k_{n,1} + k_f - \frac{k_f k_b}{k_{n,2} + k_b} = k_{n,1} + \frac{k_{n,2} k_f}{k_{n,2} + k_b}. \quad (5.14)$$

The contribution to the effective scalar coupling is,

$$2J_{eff} = 2J_1 + \frac{2k_f k_b J_2}{\left((1/2)(k_{S,2} + k_{T,2}) + k_b\right)^2 + 4J_2^2} \quad (5.15)$$

and the effective singlet-triplet dephasing rate,

$$k_{D,eff} = \frac{k_{S,1} + k_{T,1}}{2} + k_f - \frac{k_{S,eff} + k_{T,eff}}{2} - \frac{k_f k_b \left((1/2)(k_{S,2} + k_{T,2}) + k_b \right)}{\left((1/2)(k_{S,2} + k_{T,2}) + k_b \right)^2 + 4J_2^2} \quad (5.16)$$

$$k_{D,eff} = \frac{k_f k_b}{2} \left(\frac{1}{k_b + k_{S,2}} + \frac{1}{k_b + k_{T,2}} \right) - \frac{k_f k_b \left((1/2)(k_{S,2} + k_{T,2}) + k_b \right)}{\left((1/2)(k_{S,2} + k_{T,2}) + k_b \right)^2 + 4J_2^2}. \quad (5.17)$$

5.2.4 Analysis of results

Some of the electronic transitions in the molecules we have considered have been shown to have negative effective activation energies (Table 5.3). If a recombination pathway is negatively activated then this suggests that the following inequalities are valid,

$$k_b \gg k_{n,2} \quad \text{and} \quad \frac{k_f k_{n,2}}{k_b} \gg k_{n,1} \quad (5.18)$$

so that the effective rate constant for the recombination in equation 5.14 is approximately described by

$$k_{n,eff} \approx \frac{k_f k_{n,2}}{k_b}. \quad (5.19)$$

Here the activation energies of each step must satisfy $Ea_f - Ea_b + Ea_{n,2} < 0$ for an overall negative effective activation energy to be observed. If both pathways are negatively activated then this suggests that the contribution to the effective scalar coupling term is

$$2J_{eff} \approx 2J_1 + 2J_2 \left(\frac{k_f k_b}{k_b^2 + 4J_2^2} \right). \quad (5.20)$$

The scalar coupling contribution of the intermediate radical pair state is likely to be large, as seen in figure 5.3 the effective scalar coupling is significantly larger than other rate constants, so that the limit $J_2 \gg k_b$ can be applied and therefore the effective scalar coupling contribution is given by

$$2J_{eff} \approx 2J_1 + k_f \left(\frac{k_b}{J_2} \right) \approx 2J_1. \quad (5.21)$$

Consequently the temperature dependence of the effective scalar coupling term will be dominated by $J_1(T)$, the temperature dependence of the scalar coupling of the initial radical pair state. If, as is the case in these molecules, the effective scalar coupling is positively activated, most likely due to an increase in the sampling of high energy conformations which have stronger electronic coupling^[56], then the dephasing rate can also be simplified. Assuming again that $J_2 \gg k_b$,

$$k_{D,eff} \approx k_f \left(1 - \frac{k_b^2}{k_b^2 + 4J_2^2}\right) \approx k_f \left(1 - \frac{k_b^2}{4J_2^2}\right) \approx k_f. \quad (5.22)$$

The bridges for PE_1P and FN_1 are completely different structures and it would be expected that the torsional motions and therefore the dephasing rate will correspondingly be very different. However, as seen in Table 5.3, they differ by less than a factor of 2 which is consistent with $k_D \approx k_{D,eff} \approx k_f$ if k_f is similar for both molecules. This reinforces the suggestion that the intermediate radical pair state is $DMJ - An^+ - B - NDI^-$ for both molecules. The observed scalar coupling $J_{obs} = J_{eff}$ is of the order of magnitude of $10 \text{ mT} = 1.4 \times 10^8 \text{ s}^{-1}$, which is an order of magnitude greater than the dephasing rate for both molecules (i.e. $J_{eff} > k_D$). This is consistent with approximate expressions for J_{eff} and $k_{D,eff}$ given in equations 5.21 and 5.22 respectively. The dephasing has been accurately described by a constant, temperature independent, term which implies that the reaction described by k_f is only weakly temperature dependent.

The singlet recombination pathways are more negatively activated for both molecular species which implies that the transition from the intermediate triplet radical pair state is more highly activated than that from the respective singlet state. However, as observed in figure 5.3, the triplet recombination rate is between one and two orders of magnitude larger than the singlet recombination rate. This difference can not be fully accounted for by the existence of two triplet recombination pathways and therefore implies that the electronic coupling is stronger in the triplet radical pair state than the singlet. The singlet ground state is lower in energy than the triplet ground state and therefore the singlet recombination electron transition has

a higher driving force than the triplet recombination. The singlet transition is also more weakly activated which suggests that both transitions are in the Marcus normal region and the singlet transition is higher up the Marcus rate curve. The main implication of this analysis is that negatively activated effective electronic transitions occur via a more stable intermediate radical pair state. The observations of this analysis are in agreement with the properties of the proposed intermediate radical pair state $DMJ - An^+ - B - NDI^-$ which may be lower in energy than the initial radical pair due to electrostatic charge stabilisation.

5.2.5 Singlet-Triplet dephasing mechanism

Earlier it was shown that the dephasing rate in the extreme narrowing limit is given by

$$k_D = 4\tau_c \langle \Delta J \rangle^2 \quad (5.23)$$

Therefore, by estimating that ΔJ is of the same order of magnitude as J , an estimate of the correlation time τ_c can be calculated assuming k_D is dominated by this term. Taking $\Delta J = 30 \text{ mT}$ as an estimate and using the dephasing rate $k_D = 1.468 \times 10^7 \text{ s}^{-1}$ for FN_1 and $k_D = 8.972 \times 10^6 \text{ s}^{-1}$ for PE_1P then,

$$\tau_c(FN_1) = 1.43 \times 10^{-11} \text{ s} \quad (5.24)$$

$$\tau_c(PE_1P) = 2.14 \times 10^{-11} \text{ s} \quad (5.25)$$

The dephasing rate for both molecules is of the same order of magnitude as shown in Table 5.3 and is less than the exponential model's triplet recombination rate as shown in figure 5.3. This implies that the triplet radical pair recombination rate is the dominant contribution to the lifetime broadening effect which determines the peak width in the MARY curves.

It would be expected, given the very different structures of the bridging species of the molecules, that the torsional motions and therefore the correlation times would be very different for the two molecules. However the suggestion, from the previous analysis, that the transition rate to the same intermediate state dominates

the effective dephasing would resolve this issue. In the real physical system both effects will contribute and thus a slight discrepancy between the dephasing rates is observed.

5.2.6 Triplet yield correction at high fields

PE_1P - Method	Mean NSE	Mean (%) in lifetime
Initial triplet fraction	0.792	25.228
Intersystem crossing with singlet recombination	0.480	27.356
Additional relaxation	-0.910	18.513
No background	-0.138	20.181
FN_1 - Method	Mean NSE	Mean (%) in lifetime
Initial triplet fraction	0.853	6.579
Intersystem crossing with singlet recombination	0.812	25.858
Additional relaxation	-4.219	26.878
No background	-155.3	19.483

Table 5.4: Comparison of background triplet yield contributions for the exponential model.

The parameters which quantify the correction to the triplet yield at high field strengths were estimated using the maximum likelihood method for three distinct contributions. All three corrections improved the goodness of fit when compared to the model with no background field independent contribution as shown in Table 5.4.

The initial triplet fraction was estimated to be $\lambda = 0.429$ for the FN_1 molecule and $\lambda = 0.458$ for the PE_1P molecule. Both these values are very high and it would be interesting to see if experimental EPR studies agreed with these results. It is likely that these values are anomalously high because the initial triplet yield is only one factor in the real physical system which contributes to the background triplet yield.

The value x_0 for the spin-orbit coupled intersystem crossing rate which accompanies singlet recombination was estimated to equal $x_0 = 0.316$ for the FN_1 molecule and $x_0 = 0.0933$ for the PE_1P molecule. The temperature dependence is plotted for the intersystem crossing rate k_{ST} , the singlet-singlet radical pair recombination rate $k_{SS} = k_{S,obs} - k_{ST}$ and the triplet radical pair recombination rate k_T in figure 5.6

for both molecular species. Although the transitions described by k_{ST} and k_T have the same energetic driving force and activation potential, the electronic coupling matrix element for the triplet-triplet recombination is much greater than that for singlet-triplet recombination. This is observed in figure 5.6 and the difference of a couple of orders of magnitude is consistent with what would be expected for a spin forbidden transition.

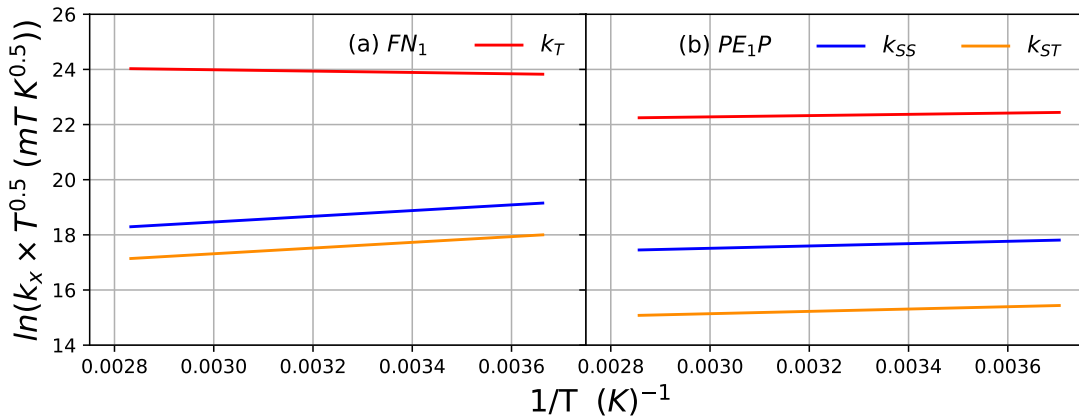


Figure 5.6: Rate constant temperature dependence with k_S and k_{ST} calculated using the exponential rate model.

The rate constant for the additional spin relaxation mechanism was found to be $k_{relax} = 0.0137 \text{ mT} = 1.928 \times 10^5 \text{ s}^{-1}$ for the FN_1 and $k_{relax} = 0.00254 \text{ mT} = 3.555 \times 10^5 \text{ s}^{-1}$ for the PE_1P molecule. Additional relaxation contributions of this order of magnitude are physically reasonable^[36] however the results, as seen by the NSE coefficient, are a poor replication of the experimental results which suggests the additional relaxation is not sufficient to explain the data. As the additional relaxation is the worst model for accounting for the background triplet yield contribution it is therefore likely to be the least significant contribution in the real physical system. Additional relaxation may arise from mechanisms including: vibrationally coupled modulations of interaction terms; the nuclear Zeeman interaction^[16]; nuclear-dipole interactions^[17]; nuclear-orbital interactions^[18]; and nuclear-quadrupolar interactions^[18] which have not been accounted for elsewhere in the model.

The goodness of fit for each model is presented in Tables 5.4 and the MARY curves and lifetimes are presented in the appendix. The initial triplet fraction model provides the results that most strongly align with the experimental data. This suggests that it may be the dominant contribution to the background triplet yield, however as mentioned, it is likely that in the real system all of these effects contribute to the observed field independent triplet yield. The intersystem crossing mechanism reproduced the experimental results more accurately than the additional relaxation, suggesting that it is a more dominant contribution. The observed importance of including a high field triplet yield contribution is consistent with the experimental findings of Wasielewski^[1] and the computational studies by Steiner^[36] and Fay^[35].

Chapter 6

Conclusion and Future work

The focus of this thesis has been to develop a method to simulate the coherent evolution of spin dynamics in the condensed phase. By using the static-bath approximation applied to Redfield theory a method has been devised in which these calculations can be performed for radical pairs with a large number of nuclear spins while accounting for relaxation effects. This new method includes asymmetric radical pair recombination ($k_S \neq k_T$) and therefore can be used to probe spin selective reactivity and charge transport. The parameters for the model were estimated using maximum likelihood estimation and the simulations were then quantitatively compared to the experimental results.

It was firstly ascertained that there was a discrepancy of many orders of magnitude between the triplet recombination rate estimated in this thesis compared to that found by the experimental researchers using a simple kinetic model. In addition to this large quantitative difference, the qualitative discrepancies between the effective activation of the rate constants in our model and those obtained using the kinetic scheme are significant. Scott *et al.*^[6] found the singlet recombination in FN_1 to be the only negatively activated process whereas the results obtained in this thesis also found the PE_1P triplet and singlet pathways to be negatively activated. This explicitly demonstrates the importance of accounting for the coherent dynamics of the singlet and triplet radical pair states in addition to incoherent spin relaxation.

Appropriate equations for the temperature dependent rate constants and reactive scalar coupling constant were successfully parameterised using the maximum-likelihood method of estimation. An analysis of the activation energies of these transitions was subsequently conducted using the Nakajima-Zwanzig formalism applied to a model for the system with an intermediate radical pair state. The proposed form of this intermediate state was substantiated by the conclusions of this analysis.

The necessity for the inclusion of mechanisms which contribute a field independent background to the triplet yield, which has been suggested previously^[35], was confirmed and the initial triplet fraction shown to be the dominant effect.

In future research it may be of interest to explore further the regimes in which the extreme narrowing limit becomes a valid approximation and quantitatively compare these results to those of stochastic Liouville theory. Furthermore the physical origin of the high field triplet contribution should be explored, for example by probing the initial triplet yield mechanism experimentally using EPR studies. The theoretical approach to modelling these systems and the code developed to do so could also be applied to model the spin dynamics of other radical pair systems of interest in biochemistry or material science.

Bibliography

- [1] Michael R. Wasielewski. *Journal of Organic Chemistry*, 71(14):5051–5066, 2006.
- [2] Brian Brocklehurst. *Chemical Society Reviews*, 31(5):301–311, 2002.
- [3] Hamish G. Hiscock, Daniel R. Kattnig, David E. Manolopoulos, and P. J. Hore. *Journal of Chemical Physics*, 145(12), 2016.
- [4] C. T. Rodgers and P. J. Hore. *Proceedings of the National Academy of Sciences*, 106(2):353–360, 2009.
- [5] Thorsten Ritz, Salih Adem, and Klaus Schulten. *Biophysical Journal*, 78(2):707–718, 2000.
- [6] Amy M Scott and Michael R Wasielewski. *Journal of the American Chemical Society*, pages 3005–3013, 2011.
- [7] Ulrich E. Steiner and Thomas Ulrich. *Chemical Reviews*, 89(1):51–147, 1989.
- [8] Christopher T. Rodgers. 2009.
- [9] Emily A. Weiss, Michael J. Ahrens, Louise E. Sinks, Alexey V. Gusev, Mark A. Ratner, and Michael R. Wasielewski. *Journal of the American Chemical Society*, 126(17):5577–5584, 2004.
- [10] P. A. M Dirac. *Proceedings of the Royal Society A: Mathematical, Physical and Engineering Sciences*, 117:610–624, 1928.
- [11] Emily A. Weiss, Mark A. Ratner, and Michael R. Wasielewski. *Journal of Physical Chemistry A*, 107(19):3639–3647, 2003.
- [12] Emily A. Weiss, Michael J. Tauber, Mark A. Ratner, and Michael R. Wasielewski. *Journal of the American Chemical Society*, 127(16):6052–6061, 2005.
- [13] Alan M. Lewis, David E. Manolopoulos, and P. J. Hore. *Journal of Chemical Physics*, 141(4), 2014.
- [14] Thomas P. Fay, Lachlan P. Lindoy, and David E. Manolopoulos. Technical report, 2019, in progress.
- [15] Dirk M. Guldi, Hiroshi Nishiharab, and Latha Venkataraman. *Chemical Society Reviews*, 44:842, 2015.
- [16] W. A. Coish and J. Baugh. *Physica Status Solidi (B) Basic Research*, 246(10):2203–2215, 2009.
- [17] Rogerio de Sousa and S. Das Sarma. *Physical Review B - Condensed Matter and Materials Physics*, 68(11):1153221–11532213, 2003.
- [18] Jan Fischer, W. A. Coish, D. V. Bulaev, and Daniel Loss. *Physical Review B - Condensed Matter and Materials Physics*, 78(15):1–9, 2008.
- [19] Carrington and McLachlan. *Harper & Row*, 1967.
- [20] Atherton. *Ellis Horwood Limited, ISBN 0470036001*, 1973.
- [21] Neese. *ORCA*, 2006.
- [22] E. Fermi. *Nature*, 125(16):287–310, 1930.
- [23] Jan Fischer, Björn Trauzettel, and Daniel Loss. *Physical Review B - Condensed Matter and Materials Physics*, 80(15):1–9, 2009.
- [24] Thomas P. Fay, Lachlan P. Lindoy, and David E. Manolopoulos. *Journal of Chemical Physics*, 149(6), 2018.
- [25] R. Haberkorn. *Molecular Physics*, 32(5):1491–1493, 1976.
- [26] J. A. Jones, Kiminori Maeda, and P. J. Hore. *Chemical Physics Letters*, 507(4-6):269–273, 2011.
- [27] Klaus Schulten and Peter G. Wolynes. *The Journal of Chemical Physics*, 68(7):3292–3297, 1978.
- [28] A.G. Redfield. *IBM Journal of Research and Development*, 1(1):19–31, 1957.
- [29] Eric W. Weisstein. <http://mathworld.wolfram.com/SpherePointPicking.html>.
- [30] Matthew P Nicholas, Ertan Eryilmaz, Fabien Ferrage, David Cowburn, and Ranajeet Ghose. 57(2):111–158, 2014.
- [31] Susannah Worster, Daniel R. Kattnig, and P. J. Hore. *Journal of Chemical Physics*, 145(3), 2016.
- [32] R. A. Marcus. *The Journal of Chemical Physics*, 24(5):966–978, 1956.
- [33] N. S. Hush. *The Journal of Chemical Physics*, 28(5):962–972, 1958.
- [34] Weiwei Zhang, Wanzhen Liang, and Yi Zhao. *Journal of Chemical Physics*, 133(2), 2010.

- [35] Thomas P. Fay, Alan M. Lewis, and David E. Manolopoulos. *Journal of Chemical Physics*, 147(6), 2017.
- [36] Ulrich E. Steiner, Julian Schäfer, Nikita N. Lukzen, and Christoph Lambert. *Journal of Physical Chemistry C*, 122(22):11701–11708, 2018.
- [37] Johannes H. Klein, David Schmidt, Ulrich E. Steiner, and Christoph Lambert. *Journal of the American Chemical Society*, 137(34):11011–11021, 2015.
- [38] Zachary E.X. Dance, Qixi Mi, David W. McCamant, Michael J. Ahrens, Mark A. Ratner, and Michael R. Wasielewski. *Journal of Physical Chemistry B*, 110(50):25163–25173, 2006.
- [39] Goja Andric, John F. Boas, Alan M. Bond, Gary D. Fallon, Kenneth P. Ghiggino, Conor F. Hogan, James A. Hutchison, Marcia A.-P. Lee, Steven J. Langford A, John R. Pilbrow, Gordon J. Troup, and Clint P. Woodward. *Australian Journal of Chemistry*, 57(10):1011–1019, 2004.
- [40] Robert I. Cukier and J.R. R. Mehafeey. *Physical Review Letters*, 38(19):1039–1042, 1977.
- [41] Yousry Hessein Adbelkader, Hatem Hamda, Aymen Messaâdi, Nesrine Dhouibi, Ahmed Hichem Hamzaoui, Fethi Bin Muhammad Belgacem, and Nouredine Ouerfelli. *Journal of Chemistry*, 2015:1–12, 2015.
- [42] William Press, Brian Flannery, Saul Teukolsky, and William Vetterling. *Technometrics*, 29(4), 2002.
- [43] Rainer Storn and Kenneth Price. *Journal of Global Optimization* 11:, 11:341–359, 1997.
- [44] J A Nelder and R Mead. *The Computer Journal*, 7(4):308–313, 1965.
- [45] E Nash and V Sutcliffe. *Journal of Hydrology*, 10:282–290, 1970.
- [46] Hakden M. McConnell. *The Journal of Chemical Physics*, 35(2):508–515, 1961.
- [47] Joshua Jortner, Mordechai Bixon, Thomas Langenbacher, and Maria E Michel-Beyerle. *Chemistry National Academy of Sciences*, 95(October):12759–12765, 1998.
- [48] Neil R. Kestner, Jean Logan, and Joshua Jortner. *Journal of Physical Chemistry*, 78(21):2148–2166, 1974.
- [49] Yuri A. Berlin, Geoffrey R. Hutchison, Pawel Rempala, Mark A. Ratner, and Josef Michl. *Journal of Physical Chemistry A*, 107(19):3970–3980, 2003.
- [50] Mélina Gilbert and Bo Albinsson. *Chemical Society Reviews*, 44(4):845–862, 2015.
- [51] Amy M. Scott, Tomoaki Miura, Annie Butler Ricks, Zachary E.X. Dance, Emilie M. Giacobbe, Michael T. Colvin, and Michael R. Wasielewski. *Journal of the American Chemical Society*, 131(48):17655–17666, 2009.
- [52] W. B. Davis, M. A. Ratner, and M. R. Wasielewski. *Journal of the American Chemical Society*, 123(32):7877–7886, 2001.
- [53] H Heitele and P Finckh. *Chemical Physics Letters*, 138(2):237–243, 1987.
- [54] Ephraim Buhks and Joshua Jortner. *FEBS Letters*, 109(1):1–3, 1979.
- [55] Shunzo Yamamoto, Tetsuo Sakurai, Liu Yingjin, and Yoshimi Sueishi. *Phys. Chem. Chem. Phys.*, 1:833–837, 1999.
- [56] Emily A. Weiss, Michael J. Tauber, Richard F. Kelley, Michael J. Ahrens, Mark A. Ratner, and Michael R. Wasielewski. *Journal of the American Chemical Society*, 127(33):11842–11850, 2005.

Appendix A

Redfield theory in Liouville space

The general equation for the Redfield Superoperator that has been derived is

$$\mathcal{R} = - \sum_{j,k} \int_0^\infty d\tau g_{j,k}(\tau) \hat{\mathcal{A}}_j^{I\dagger} e^{+\mathcal{L}_0\tau} \hat{\mathcal{A}}_j^I e^{-\mathcal{L}_0\tau} \quad (\text{A.1})$$

For the reference Liouville superoperator \mathcal{L}_0 which does not preserve pure states the expression is evaluated by finding the eigenvectors \mathcal{P} , \mathcal{P}^{-1} and eigenvalues (λ) for \mathcal{L}_0 in Liouville space,

$$e^{+\mathcal{L}_0} = \mathcal{P} e^{+\lambda} \mathcal{P}^{-1}. \quad (\text{A.2})$$

Hence the Redfield superoperator can now be written in terms of the eigenvalues and eigenvectors of the reference Liouvillian,

$$\mathcal{R} = - \sum_{j,k} \int_0^\infty d\tau g_{j,k}(\tau) \hat{\mathcal{A}}_j^{I\dagger} \mathcal{P} e^{+\lambda\tau} \mathcal{P}^{-1} \hat{\mathcal{A}}_j^I \mathcal{P} e^{-\lambda\tau} \mathcal{P}^{-1} \quad (\text{A.3})$$

The spectral density function is defined as the complex Fourier transform of the correlation functions is given by

$$J_{j,k}(z) = \int_0^\infty g_{j,k}(\tau) e^{iz\tau} d\tau. \quad (\text{A.4})$$

By evaluating each component $[\mathcal{R}_{j,k}]_{a,b}$ in terms of the spectral density function the matrix can be computed using the equation

$$\mathcal{R}_{j,k} = -\hat{\mathcal{A}}_j^{I\dagger} \mathcal{P} \sum_{a,b,c,d} \left[\int_0^\infty d\tau g_{j,k}(\tau) e^{+\lambda_{a,c}\tau} \right] \left[\mathcal{P}^{-1} \hat{\mathcal{A}}_j^I \mathcal{P} \right]_{c,d} \left[e^{-\lambda_{d,b}\tau} \right] \mathcal{P}^{-1}. \quad (\text{A.5})$$

However, only the diagonal elements of the matrix of eigenvalues λ are non-zero and consequently the summations can be reduced from being over four to two variables.

The matrix elements are therefore given by

$$\mathcal{R}_{j,k} = -\hat{\mathcal{A}}_j^{I\dagger} \mathcal{P} \sum_{a,b} \left[\int_0^\infty d\tau g_{j,k}(\tau) e^{+\lambda_a\tau} \right] \left[\mathcal{P}^{-1} \hat{\mathcal{A}}_j^I \mathcal{P} \right]_{a,b} \left[e^{-\lambda_b\tau} \right] \mathcal{P}^{-1}. \quad (\text{A.6})$$

The components can be permuted such that the matrix elements are given by

$$\mathcal{R}_{j,k} = -\hat{\mathcal{A}}_j^{I\dagger} \mathcal{P} \sum_{a,b} \left[\int_0^\infty d\tau g_{j,k}(\tau) e^{+(\lambda_a - \lambda_b)\tau} \right] \left[\mathcal{P}^{-1} \hat{\mathcal{A}}_j^I \mathcal{P} \right]_{a,b} \mathcal{P}^{-1}. \quad (\text{A.7})$$

A matrix of spectral densities $\mathcal{J}_{j,k}$ is now defined in terms of its matrix elements by

$$\left[\mathcal{J}_{j,k}\right]_{a,b} = J_{j,k}\left(i(\lambda_b - \lambda_a)\right) \quad (\text{A.8})$$

and the final expression is obtained by substituting in this spectral density matrix and taking the inner product to give

$$\mathcal{R} = - \sum_{j,k} \mathcal{A}_j^I{}^\dagger \mathcal{P} \left(\mathcal{J}_{j,k} \circ (\mathcal{P}^{-1} \mathcal{A}_k^I \mathcal{P}) \right) \mathcal{P}^{-1} \quad (\text{A.9})$$

where \circ is the element wise product.

Appendix B

Extended Marcus-Hush theory

This appendix presents the extended Marcus-Hush theory and its parameters for PE_1P and FN_1 estimated using the maximum likelihood method. The simulations using this model are shown in Appendix C.

Marcus-Hush theory predicts that the rate of electron transfer is given by

$$k_X = \left(\frac{\Delta_X^2}{\hbar}\right) \left(\sqrt{\frac{\pi}{k_b T \lambda_X}}\right) e^{-(\lambda_X - \epsilon_X)^2 / (4\lambda_X k_b T)} \quad (\text{B.1})$$

where $X = S$ or T for the singlet and triplet recombination rates respectively. Here ϵ_X is the negative of the free energy difference between the singlet or triplet radical pair and product states and $\Delta_X = \Delta_S$ or Δ_T is the diabatic coupling between these states^{[32][33]}. λ_x is the reorganisation energy for the transition from the singlet and triplet states. Recently a formalism for the reactive scalar electron spin coupling has been developed which, in the non-adiabatic limit, is dependent only upon the parameters which appear in the Marcus-Hush rate expression^[24]. This contribution is found to be non negligible in many regimes and is given by the equation

$$J_X = \left(\frac{\Delta_X^2}{4}\right) \left(\sqrt{\frac{\pi}{k_b T \lambda_X}}\right) F((\epsilon_X - \lambda_X) / (2\sqrt{k_b T \lambda_X})). \quad (\text{B.2})$$

Here the Dawson F-function is defined in terms of the imaginary error function as,

$$F((\epsilon_X - \lambda_X) / (2\sqrt{k_b T \lambda_X})) = e^{-(\lambda_X - \epsilon_X)^2 / (4\lambda_X k_b T)} \operatorname{erfi}\left(\frac{\epsilon_X - \lambda_X}{2\sqrt{k_b T \lambda_X}}\right). \quad (\text{B.3})$$

The free parameters which to be estimated in the calculations are a_S , b_S , a_T , b_T and c such that

$$k_X(T) = \frac{a_X(1 + c \times T)}{\sqrt{T}} e^{-(b_X)^2 / (T)} \quad (\text{B.4})$$

$$J_X(T) = \frac{a_X(1 + c \times T)}{2 \times \sqrt{\pi T}} F\left(\frac{b_X}{\sqrt{T}}\right). \quad (\text{B.5})$$

Due to non-Condon effects, where the electronic coupling is explicitly dependent upon the nuclear coordinates, it is also necessary to include an additional temperature-dependent contribution to the J-coupling Δ_X^2 parameter. Additional coupling J_0 is

also added with the same temperature-dependence.

$$J(T) = J_S(T) - J_T(T) + J_0(1 - c \times T). \quad (\text{B.6})$$

Table D.3 displays the parameters obtained using maximum likelihood estimation for the Marcus-Hush rate equation which is defined by equations B.4 and B.5.

Molecule	$a_T (K^{\frac{1}{2}} mT)$	$b_T (K^{\frac{1}{2}})$	$a_S (K^{\frac{1}{2}} mT)$	$b_S (K^{\frac{1}{2}})$
FN_1	9270	28.6	7.15	10.8
PE_1P	2920	30.4	15.0	27.0

Molecule	$J_0 (mT)$	$c (K^{-1})$	λ	$k_D (s^{-1})$
FN_1	21.0	-0.00253	0.408	1.44×10^7
PE_1P	6.57	-0.00256	0.469	1.55×10^7

Table B.1: Fitted parameters for the Marcus-Hush model.

Appendix C

Summary of models

In this appendix alternative models are explored including non-condon effects. A whole set of models have been explored which include different approaches to

Model	Rate Law	Dephasing	Background
A	Exponential	-	-
<i>Equation</i>	4.10,4.11	-	-
<i>Parameters</i>	$\alpha_S, E_S, \alpha_T, E_T, J_a, J_b$	-	-
B	Exponential	Constant	-
<i>Equation</i>	4.10,4.11	4.6	-
<i>Parameters</i>	$\alpha_S, E_S, \alpha_T, E_T, J_a, J_b$	k_D	-
C	Exponential	-	Initial triplet
<i>Equation</i>	4.10,4.11	-	4.12
<i>Parameters</i>	$\alpha_S, E_S, \alpha_T, E_T, J_a, J_b$	-	λ
D	Exponential	Constant	Initial triplet
<i>Equation</i>	4.10,4.11	4.6	4.12
<i>Parameters</i>	$\alpha_S, E_S, \alpha_T, E_T, J_a, J_b$	k_D	λ
E	Exponential	Constant	Additional relaxation
<i>Equation</i>	4.10,4.11	4.6	4.15
<i>Parameters</i>	$\alpha_S, E_S, \alpha_T, E_T, J_a, J_b$	k_D	k_{ISC}
F	Exponential	Constant	ISC
<i>Equation</i>	4.10,4.11	4.6	4.14
<i>Parameters</i>	$\alpha_S, E_S, \alpha_T, E_T, J_a, J_b$	k_D	x_0
G	Exponential	Arrhenius	Initial triplet
<i>Equation</i>	4.10,4.11		4.12
<i>Parameters</i>	$\alpha_S, E_S, \alpha_T, E_T, J_a, J_b$	Ea_D	λ
H	Marcus-Hush	Constant	Initial triplet
<i>Equation</i>	B.4, B.5	4.6	4.12
<i>Parameters</i>	$a_S, b_S, a_T, b_T, c, J_0$	k_D	λ

Table C.1: Summary of models.

modelling the rate laws, background triplet yield and singlet-triplet dephasing rate. It is not known which contribution dominates the field independent triplet yield therefore each potential mechanism will be used in a different model. The two distinct sets of rate laws form two distinct models as it is not known which will better approximate the temperature dependence of the spin selective radical pair

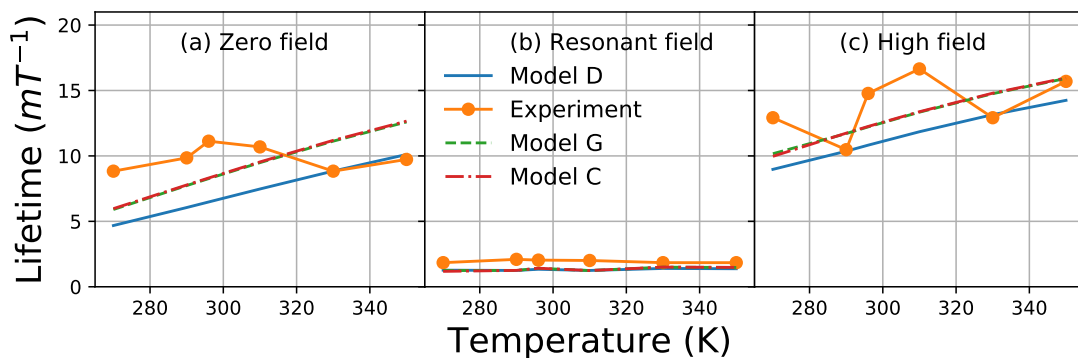
recombination rate constants and the scalar coupling constant. The significance of the temperature dependent component of the dephasing rate will also be assessed. Table C.1 presents the models and the corresponding parameters which will be estimated using the maximum likelihood method. This appendix tabulates the mean NSE and percentage difference in lifetime for each model in Tables C.3 and C.2 in addition to graphically displaying the fitted data.

Model	Mean NSE	Mean (%) difference in lifetime
A	-276.6	18.960
B	-155.3	19.483
C	0.748	4.616
D	0.853	6.570
E	-4.219	26.878
F	0.812	25.858
G	0.852	6.439
H	0.797	8.949

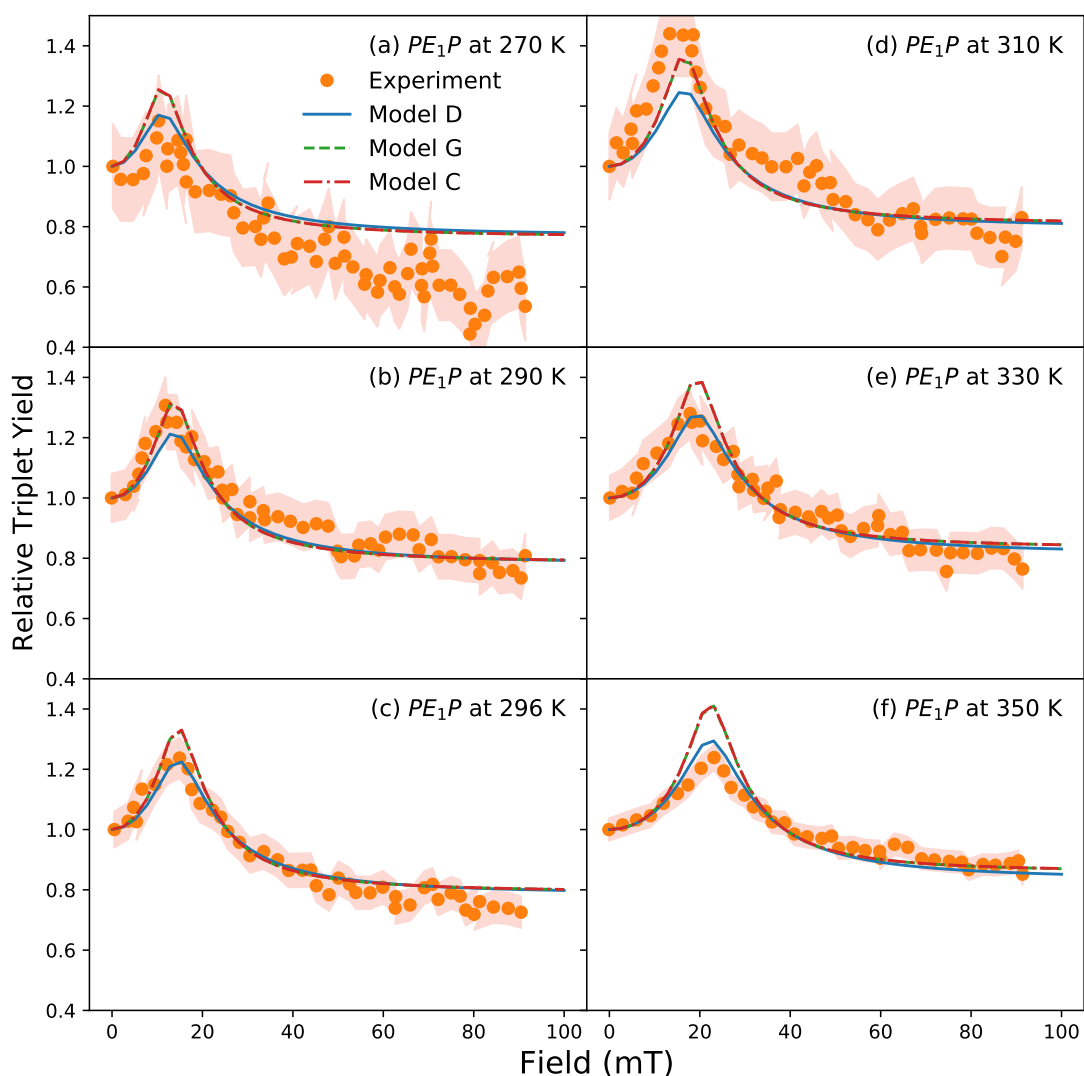
Table C.2: Quantitative evaluation of model fitting for FN_1 .

Model	Mean NSE	Mean (%) difference in lifetime
A	-0.217	21.267
B	-0.138	20.181
C	0.812	25.574
D	0.792	25.228
E	-0.910	18.513
F	0.480	27.356
G	0.747	22.893
H	0.753	28.244

Table C.3: Quantitative evaluation of model fitting for PE_1P .

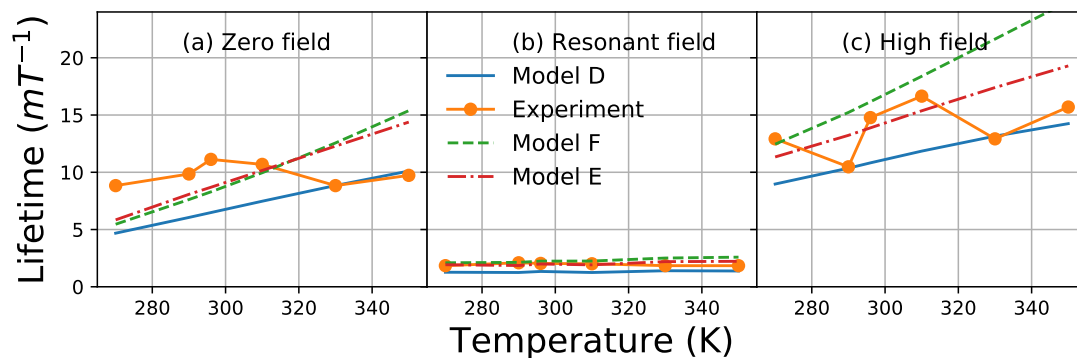


(a) Radical pair lifetimes

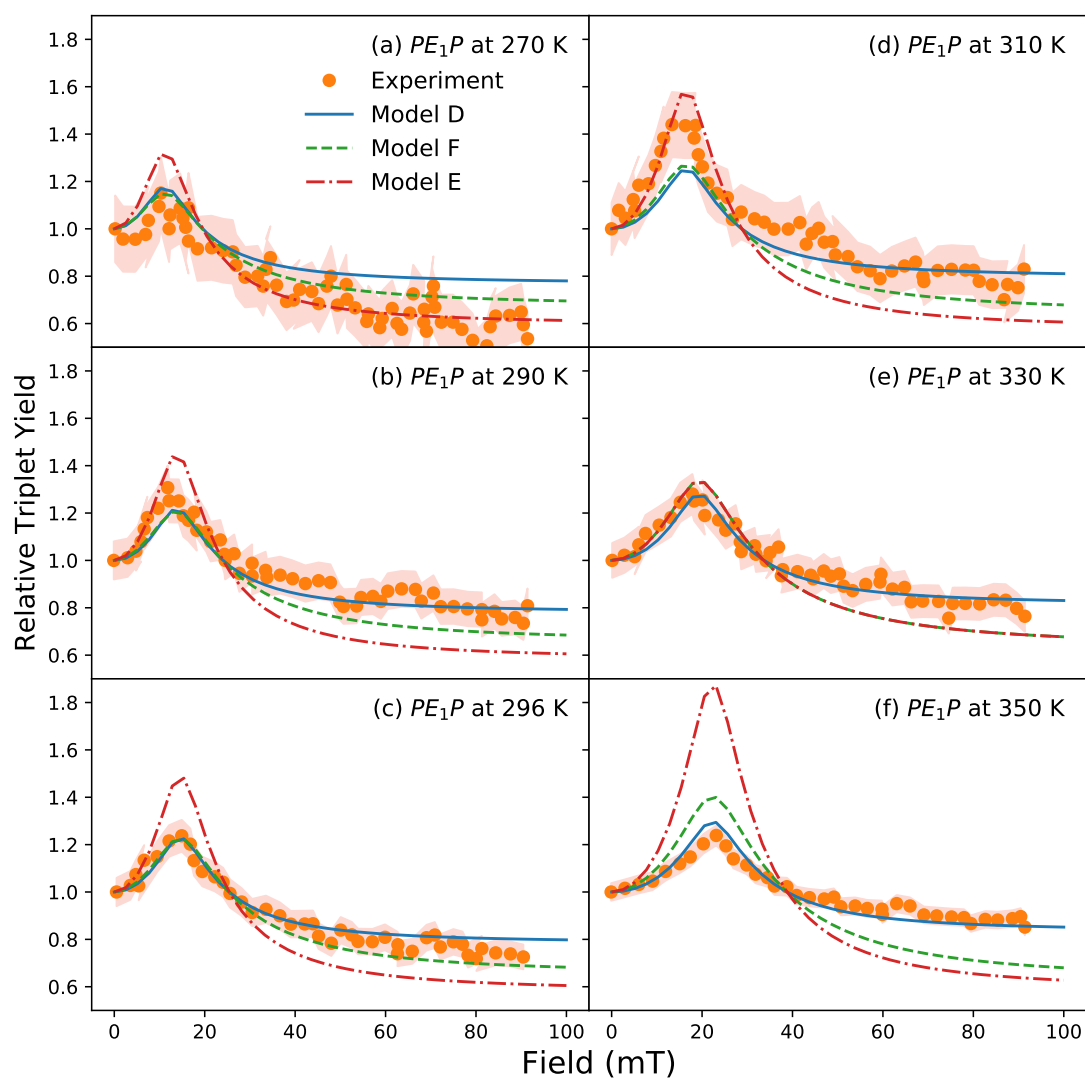


(b) MARY curves, the shaded area represents an estimate for two standard errors at each experimental data point.

Figure C.1: Comparison of Model C, Model D, Model G and experimental results for PE_1P molecule.

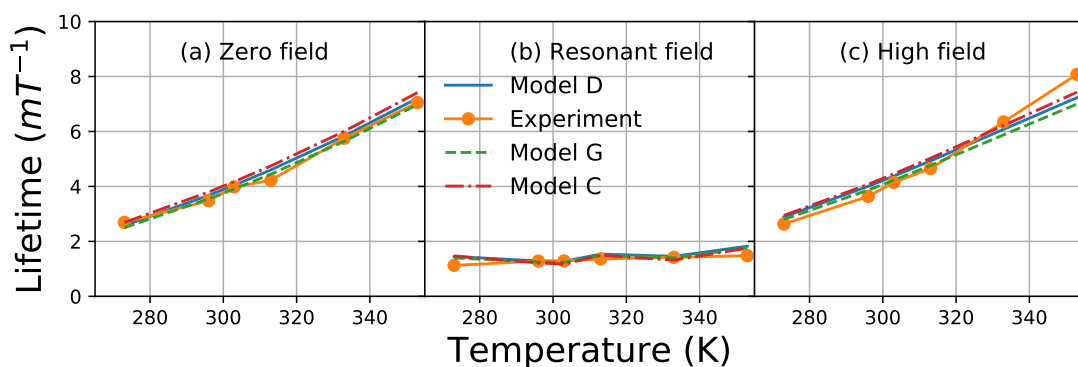


(a) Radical pair lifetimes

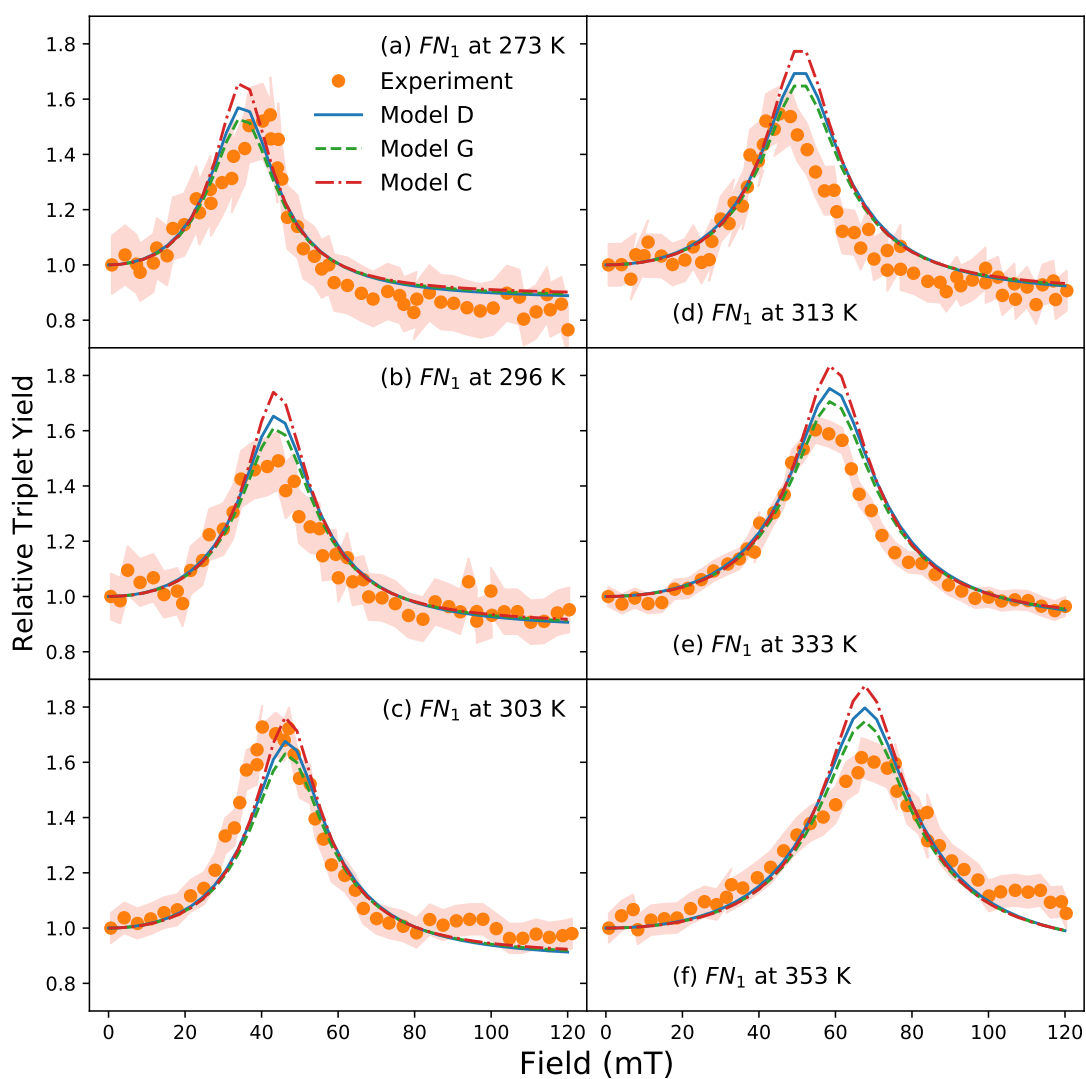


(b) MARY curves, the shaded area represents an estimate for two standard errors at each experimental data point.

Figure C.2: Comparison of Model D, Model E, Model F and experimental results for PE_1P molecule.

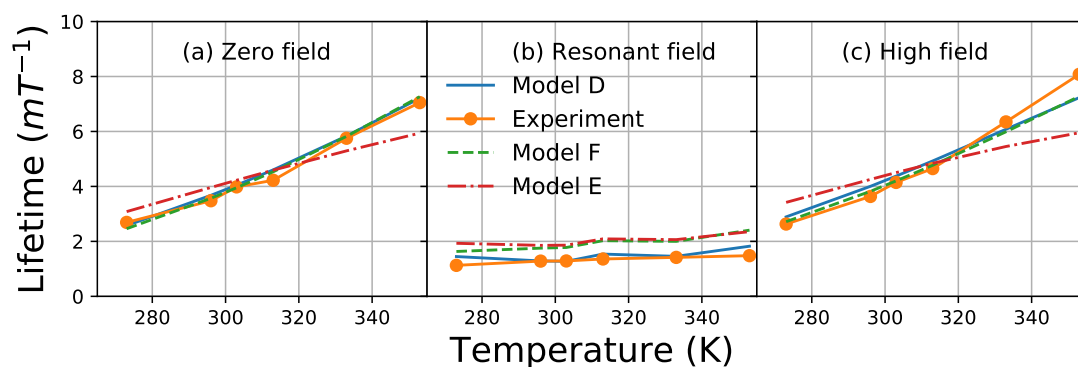


(a) Radical pair lifetimes

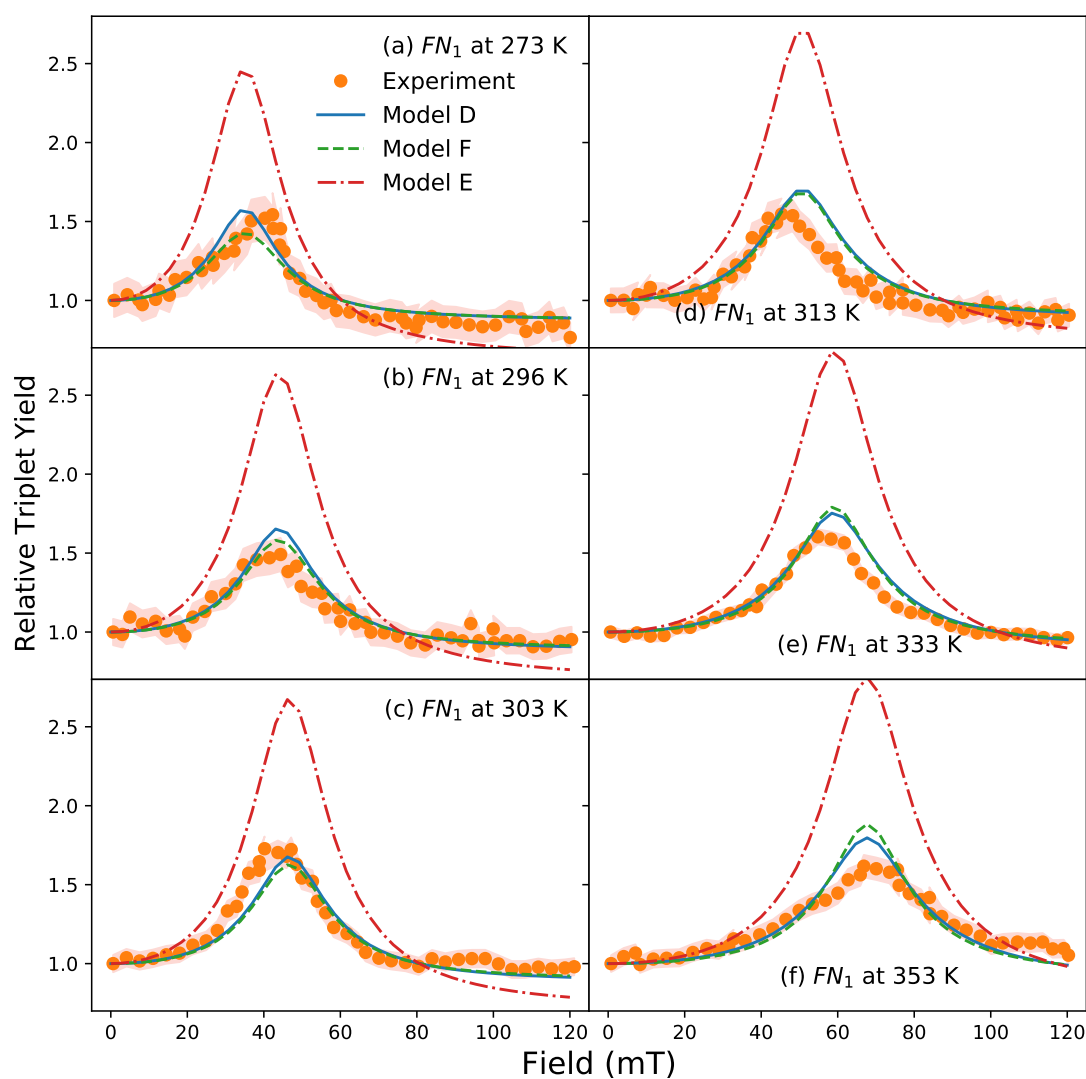


(b) MARY curves, the shaded area represents an estimate for two standard errors at each experimental data point.

Figure C.3: Comparison of Model C, Model D, Model G and experimental results for FN_1 molecule.

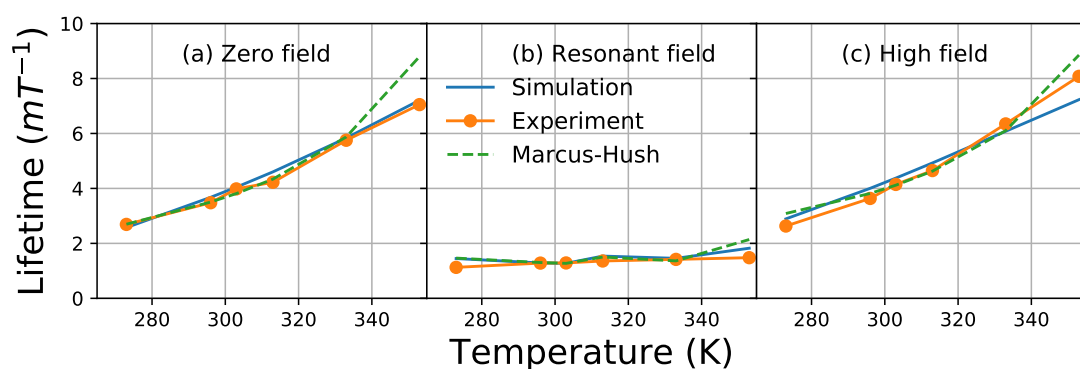


(a) Radical pair lifetimes

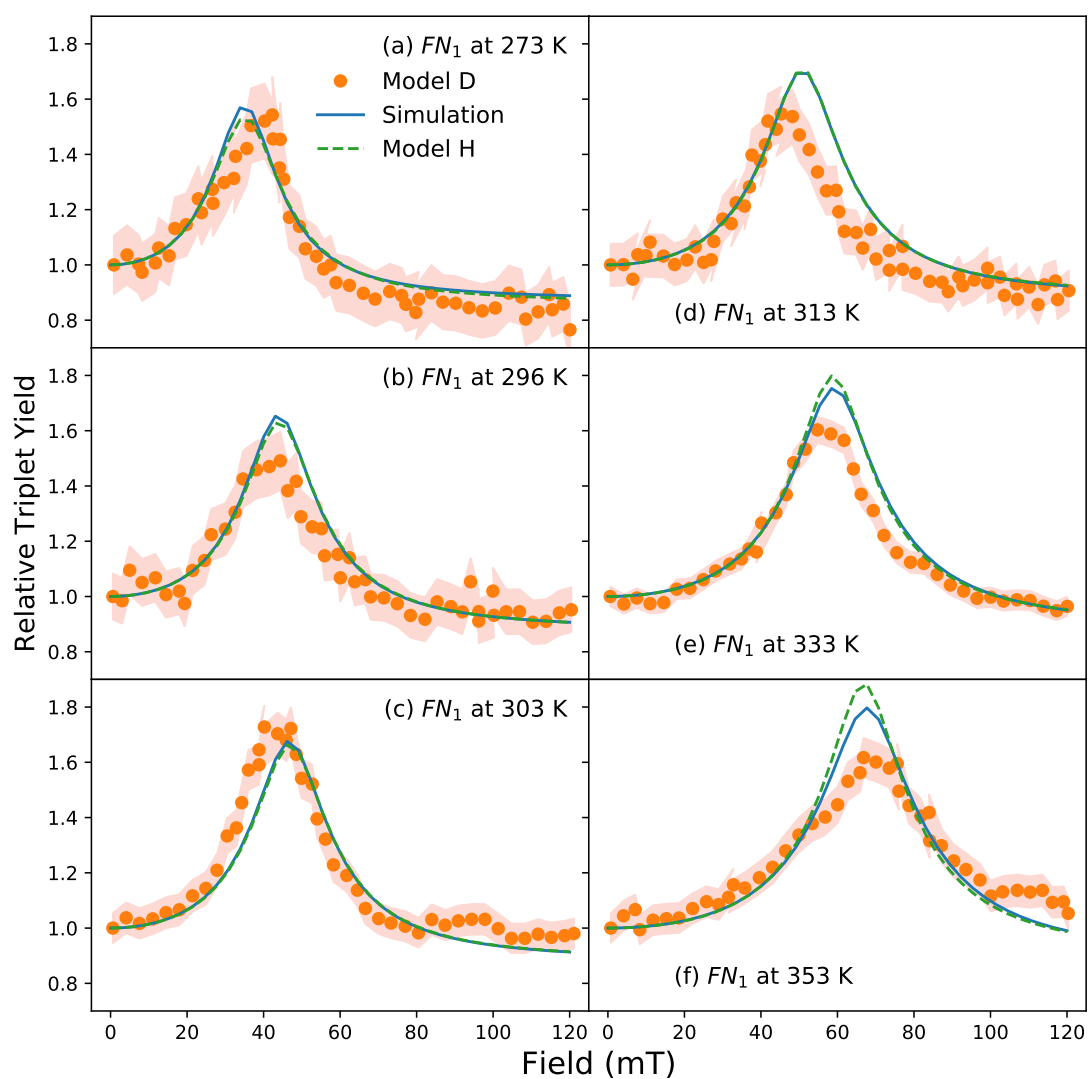


(b) MARY curves, the shaded area represents an estimate for two standard errors at each experimental data point.

Figure C.4: Comparison of Model D, Model E, Model F and experimental results for FN_1 molecule.

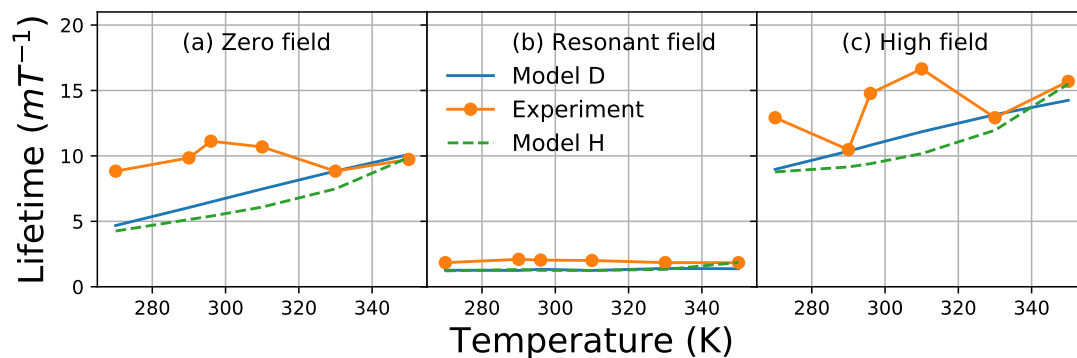


(a) Radical pair lifetimes

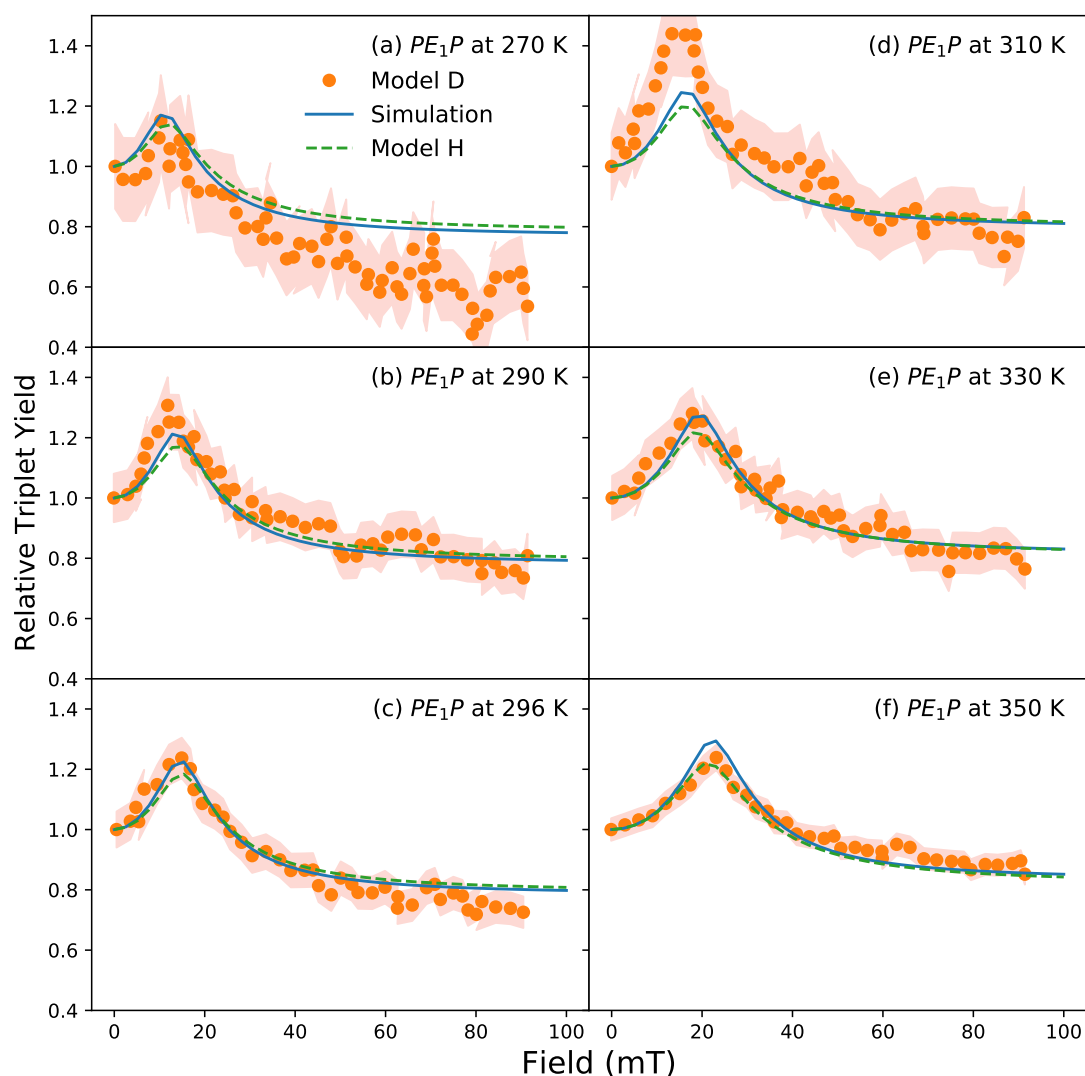


(b) MARY curves, the shaded area represents an estimate for two standard errors at each experimental data point.

Figure C.5: Comparison of rate laws, Model D and Model H, and experimental results for FN_1 molecule.



(a) Radical pair lifetimes



(b) MARY curves, the shaded area represents an estimate for two standard errors at each experimental data point.

Figure C.6: Comparison of rate laws, Model D and Model H, and experimental results for PE_1P molecule.

Appendix D

Parameters from DFT calculations

This appendix presents the anisotropic Hyperfine and g-tensor components for the radical species discussed in this thesis, calculated using DFT by Tom Fay^[14].

D.1 Rotational diffusion

The rotational diffusion coefficients were calculated using the Stokes-Einstein equation^[40],

$$D_\alpha = \frac{k_B T}{8\pi\eta r_\alpha^3}, \quad (\text{D.1})$$

where $\alpha = \parallel$ or \perp and $r_\parallel = 4.906 \times 10^{-10}$ m and $r_\perp = 16.656 \times 10^{-10}$ m for FN_1 and $r_\parallel = 8.130 \times 10^{-10}$ m and $r_\perp = 16.604 \times 10^{-10}$ m for PE_1P . The parameter η is the dynamic viscosity of the solution.

D.2 Dipolar coupling tensors

Dipolar coupling tensors are calculated using the point dipole approximation, assuming two radicals lie on the molecular z-axis and taking the gyromagnetic ratio to be equal to that of a free electron. In the principal axis frame (P.A.F.) the dipolar coupling tensor is given by

$$\hat{\mathbf{D}}_{(P.A.F.)} = \left(-\frac{\mu_0 \gamma_e^2 \hbar^2}{4\pi r_{S_1, S_2}^3} \right) \begin{bmatrix} 1 & 0 & 0 \\ 0 & 1 & 0 \\ 0 & 0 & -2 \end{bmatrix}. \quad (\text{D.2})$$

where $r_{S_1, S_2} = 20.986 \times 10^{-10}$ m for FN_1 and $r_{S_1, S_2} = 24.044 \times 10^{-10}$ m for PE_1P .

D.3 G-tensors

Radical	g_{iso}	$g_{xx} - g_{iso}$	$g_{yy} - g_{iso}$	$g_{zz} - g_{iso}$
NDI_{-}	2.0040	0.0010	0.0007	-0.0020
DMJ_{+}	2.0031	0.0006	0.0001	-0.0009

Table D.1: g-tensor components used in the simulation in mT .

D.4 Hyperfine tensors

Nucleus	a_{iso}	A_{xx}^{aniso}	A_{yy}^{aniso}	A_{zz}^{aniso}	A_{xy}^{aniso}	A_{xz}^{aniso}	A_{yz}^{aniso}
H1	-0.1927	0.011586	0.032114	-0.0437	-0.101834	-0.000008	0.000014
H2	-0.1927	0.011586	0.032114	-0.0437	-0.101834	0.000014	0.000008
H3	-0.1927	0.011586	0.032114	-0.0437	-0.101834	0.000014	0.000008
H4	-0.1927	0.011586	0.032114	-0.0437	-0.101834	-0.000008	0.000014
N1	-0.0963	0.0352	0.034	-0.0692	0.0	0.0	0.0
N2	-0.0963	0.0352	0.034	-0.0692	0.0	0.0	0.0

Table D.2: Hyperfine coupling parameters for the $NDI^{\cdot-}$ radical in mT .

Nucleus	a_{iso}	A_{xx}^{aniso}	A_{yy}^{aniso}	A_{zz}^{aniso}	A_{xy}^{aniso}	A_{xz}^{aniso}	A_{yz}^{aniso}
H1	2.30884	0.01839	0.0058	-0.02414	0.11917	-0.09026	-0.10553
H2	0.90377	-0.03026	0.13477	-0.10451	0.11118	0.0395	0.06569
H3	-0.03404	0.04133	-0.03929	0.00203	0.01796	0.7892	0.02562
H4	-0.07758	0.06562	-0.01615	-0.04946	0.03666	0.01422	0.00405
H5	1.07186	0.06909	-0.05490	-0.01419	0.01375	-0.07598	-0.00648
H6	0.25883	0.09831	-0.04111	-0.057	-0.02464	0.01396	0.00280
H7	2.30829	0.01784	0.00618	-0.02403	-0.11910	-0.09007	0.10566
H8	0.90229	-0.03078	0.13541	-0.10463	-0.11088	0.03932	-0.06561
H9	-0.03420	0.04124	-0.03917	-0.00206	-0.01815	0.07890	-0.02584
H10	-0.07765	0.06542	-0.01596	-0.04936	-0.03687	0.01422	-0.00408
H11	1.073569	0.06910	-0.05490	-0.01420	-0.01404	-0.07598	0.00662
H12	0.25988	0.09846	-0.04125	-0.057122	0.02435	0.01405	-0.00281
H13	-0.16656	0.03616	-0.0003	-0.03590	0.03826	-0.00703	-0.00405
H14	-0.16656	0.03616	-0.0003	-0.03590	0.03826	-0.00703	-0.00405
H15	-0.16656	0.03616	-0.0003	-0.03590	0.03826	-0.00702	-0.00405
H16	-0.16649	0.03598	-0.00010	-0.03588	-0.03834	-0.00702	0.00407
H17	-0.16649	0.03598	-0.00010	-0.03588	-0.03834	-0.00702	0.004067
H18	-0.16649	0.03598	-0.00010	-0.03588	-0.03834	-0.00702	0.00407
N1	0.83126	-0.77268	-0.7811	1.55378	0.00000	-0.06148	0.00044

Table D.3: Hyperfine coupling parameters for the $DMJ^{\cdot+}$ radical in the anti conformation in mT .